frontiers | Frontiers in Astronomy and Space Sciences

TYPE Original Research
PUBLISHED 05 February 2026
DOI 10.3389/fspas.2025.1693302

OPEN ACCESS

EDITED BY
Scott M. Perl,
University of California, Los Angeles,
United States

REVIEWED BY
Roberto Barbieri,
University of Bologna, Italy
Svetlana Shkolyar,
University of Maryland, United States
Ashley Murphy,
Planetary Science Institute, United States

*CORRESPONDENCE
C. Tebes-Cayo,
ctebes@ucn.cl
C. Demergasso,
cdermerga@ucn.cl

RECEIVED 26 August 2025
REVISED 08 November 2025
ACCEPTED 09 December 2025
PUBLISHED 05 February 2026

CITATION
Tebes-Cayo C, Demergasso C, Cabestrero Ó, Chong G, Carrizo D, Sánchez-García L, Parro V, Warren-Rhodes K, Cabrol N, Echeverría-Vega A, Castro-Nallar E, Menzies A and Sanz-Montero ME (2026) Gypsum as a repository of extinct and extant biosignatures at Salar de Pajonales, northern Chile. *Front. Astron. Space Sci.* 12:1693302. doi: 10.3389/fspas.2025.1693302

Gypsum as a repository of extinct and extant biosignatures at Salar de Pajonales, northern Chile

C. Tebes-Cayo[1,2]*, C. Demergasso[2]*, Ó. Cabestrero[2,3], G. Chong[1], D. Carrizo[4], L. Sánchez-García[4], V. Parro[4], K. Warren-Rhodes[5], Nathalie Cabrol[5], A. Echeverría-Vega[6], Eduardo Castro-Nallar[7], A. Menzies[1,8] and M. E. Sanz-Montero[3]

[1]Departamento de Ciencias Geológicas, Facultad de Ingeniería y Ciencias Geológicas, Universidad Católica del Norte, Antofagasta, Chile, [2]Centro de Biotecnología Alberto Ruíz, Universidad Católica del Norte, Antofagasta, Chile, [3]Departamento de Mineralogía y Petrología, Facultad de Ciencias Geológicas, Universidad Complutense de Madrid, Madrid, Spain, [4]Centro de Astrobiología (CAB), CSIC-INTA, Madrid, Spain, [5]SETI Institute, Carl Sagan Center, Mountain View, CA, United States, [6]Centro de Investigación de Estudios Avanzados del Maule (CIEAM), Vicerrectoría de Investigación y Postgrado, Universidad Católica del Maule, Talca, Chile, [7]Centro de Ecología Integrativa & Instituto de Ciencias Biológicas, Universidad de Talca, Talca, Chile, [8]Bruker Nano Analytics, Berlin, Germany

Terraces near Flamencos Lagoon in the southeastern Salar de Pajonales (Chile), located at 3,517 m above sea level in the arid Altiplano, host relic gypsum stromatolites and crusts formed under extreme desiccation, intense solar radiation, and episodic hydration. These gypsum-rich environments provide a natural analog for Martian evaporitic settings, where habitability and biosignature preservation may coexist. By combining meteorological, geochemical, isotopic, and microbiological data from 19 gypsum-dominated microhabitats, we identified strong environmental controls on mineral formation and microbial community structure. Climate data confirmed prolonged aridity punctuated by potential short-lived wetting events, which provided conditions favorable for microbial reactivation and long-term biosignature retention within gypsum. Fossil stromatolites exhibited laminated fabrics, micritic filaments, and Fe-Si-rich laminae, together with diatom frustules, indicating long-term biosignature entrapment. Microbial diversity varied with mineralogy and moisture availability: stromatolites hosted specialized cyanobacteria and archaea, whereas crusts and sediments contained more diverse photoautotrophic and heterotrophic assemblages. Lipid biomarkers and $\delta^{13}C$ signatures indicated active carbon fixation *via* the Calvin cycle, dominated by cyanobacteria, photoautotrophs, and archaea in gypsum stromatolites and crusts. Fluorescence signals of *chlorophyll a* and carotenoids confirmed photosynthetic activity in near-surface layers. In contrast, signatures of the reverse tricarboxylic acid cycle were less common in gypsum samples and were mostly restricted to unconsolidated sediments near the lagoon. Overall, the gypsum evaporitic systems of the Salar de Pajonales preserve both molecular and morphological biosignatures while sustaining microbial life under extreme conditions. The spatial separation between fossil and extant signatures

underscores gypsum's exceptional capacity to entomb and protect biological evidence, reinforcing its importance as a prime target for astrobiological exploration on Mars.

KEYWORDS

gypsum, endoliths, diatoms, Salar de Pajonales, Cyanobacteria

Introduction

Gypsum, a calcium sulfate dihydrate ($CaSO_4{\cdot}2H_2O$), is one of the most abundant sulfate minerals in the Earth's crust and plays a key role in the global sulfur cycle (Van Driessche et al., 2019). It commonly forms in evaporitic environments (Rouchy and Monty, 2000; Warren, 2006) through physical, chemical, and/or biological interactions (Allwood et al., 2013), and its presence is a key indicator of paleoenvironmental conditions both on Earth and Mars.

Among the notable outcomes of microbe-mineral interactions are stromatolites, organic sedimentary structures formed through the trapping, binding, and/or precipitation of sediments resulting from the growth and metabolic activity of microorganisms (Awramik et al., 1976; Burne and Moore, 1987). These structures record some of the earliest known life forms on Earth, dating back approximately 3.5 billion years (Schopf et al., 2012), and are typically associated with Cyanobacteria within microbial laminae. In contrast, the appearance of the earliest eukaryotic algae (chlorophytes) is believed to have emerged around 750 million years ago (Butterfield, 2004; Knoll et al., 2006), marking a significant transition from microbial dominance to the gradual diversification of eukaryotic life. While carbonate stromatolites have been widely studied in the context of early life, ancient gypsum deposits are relatively scarce, likely due to the difficulty of this mineral persisting over geological timescales (Van Driessche et al., 2019).

Nevertheless, gypsum can host organic chemical biosignatures across stratified layers in the geological records and may be shaped by microbial deposition and diagenesis (Rouchy and Monty, 2000; Sanz-Montero et al., 2006; Schopf et al., 2012; Taher, 2014). The diagenesis of Messinian (6 Ma) gypsum stromatolites from Cyprus and Crete has revealed two distinct types based on their composition: fine-grained aggregates and transparent selenite crystals. The former includes columnar and domical stromatolites, while the latter consists of microbial laminae and columnar stromatolites with selenitic crystals. Within these gypsum deposits, the most promising sites for preserved microfossils and microtextures are found in beds of large crystals with syntaxial growth or near the sediment-water interface rather than in fine-grained gypsum crystals (Allwood et al., 2013). Despite challenges in distinguishing structures formed under abiotic processes from those influenced by microbial activity, several approaches have been used to study organic matter-influenced gypsum deposits by examining crystal textures, growth habits, and mineral-microbe interactions (Cody and Cody, 1988; Vogel et al., 2010; Cabestrero and Sanz-Montero, 2016; Cabestrero et al., 2022).

Stromatolites have persisted from ancient to modern times (Perri and Spadafora, 2011), and modern gypsum-rich habitats support diverse microbial life. Cyanobacteria, alongside various other microorganisms such as diatoms (Demergasso et al., 2003; Petrash et al., 2012; Benison and Karmanocky, 2014; Taher, 2014; Culka et al., 2017; Jehlička et al., 2024), heterotrophs (DiRuggiero et al., 2013; Rasuk et al., 2014; Rhind et al., 2014; Wierzchos et al., 2015), and fungi (Hughes and Lawley, 2003; Ziolkowski et al., 2013a; Cámara et al., 2016; Culka et al., 2017), have been identified in gypsum fissures and pores in polar to hyperarid climates (Supplementary Table S1). These microorganisms can survive at depths of 2–8 mm below the mineral surface, where they are potentially protected from UV radiation and desiccation, while still receiving enough light for photosynthesis (Taher, 2014) and nutrients, including water from minerals (Wierzchos et al., 2015; Huang et al., 2020).

In northern Chile, gypsum is one of the most common evaporite minerals (Chong-Díaz et al., 2020), covering larger areas than halite deposits (Risacher et al., 2003). Examples of microbial communities in habitable gypsum structures in the Atacama Desert include selenite crystals (Benison and Karmanocky, 2014), gypsum deposits (Ziolkowski et al., 2013b), evaporites (Demergasso et al., 2003; Rasuk et al., 2014; Reid et al., 2021), and alabaster (Warren-Rhodes et al., 2023).

One of the most compelling analogs for studying microbial life in extreme gypsum environments is the Salar de Pajonales (SP), an Andean Salt Flat at 3,517 m a.s.l. in northern Chile (25°10′S, 68°49′W; Figure 1). Its geological setting includes Miocene rhyolites from the Río Frío and Pajonales Ignimbrite formations (Risacher et al., 2003). To the east, the basin is demarcated by volcanoes dating from the Miocene to Lower Pliocene age (Naranjo et al., 2013). These volcanic inputs contribute solutes that favor the precipitation of evaporites throughout the basin. SP contains a variety of shallow brine environments, including lagoons sustained by snowmelt, rainfall, and groundwater discharge (Rodríguez, 2018). The precipitated minerals are primarily composed of gypsum, along with halite, calcite, and smaller amount of ulexite (Chong-Díaz et al., 2020). Its landscape includes extensive gypsum terraces, surface crusts, lagoons, and polygonal ridges, with microbial colonization particularly evident around Flamencos Lagoon in the southeastern sector (Rodríguez, 2018; Ercilla, 2019; Hinman et al., 2022). The basin experiences extreme climatic conditions but lacks long-term meteorological records from local weather stations due to its isolation, absence of permanent inhabitants, and limited accessibility (Benison, 2019). However, available data indicate scarce low annual precipitation approximately ~150 $mm{\cdot}yr^{-1}$, low average temperatures around 5 °C, and high evaporation rates up to 1,350 $mm{\cdot}yr^{-1}$ (Risacher et al., 1999), combined with some of the highest solar radiation fluxes on Earth, ca. 310 $W{\cdot}m^{-2}$, reaching up to 6.6 $kWh{\cdot}m^{-2}{\cdot}d^{-1}$ (Kampf and Tyler, 2006; Duffie and Beckman, 2013). These conditions make SP an ideal natural

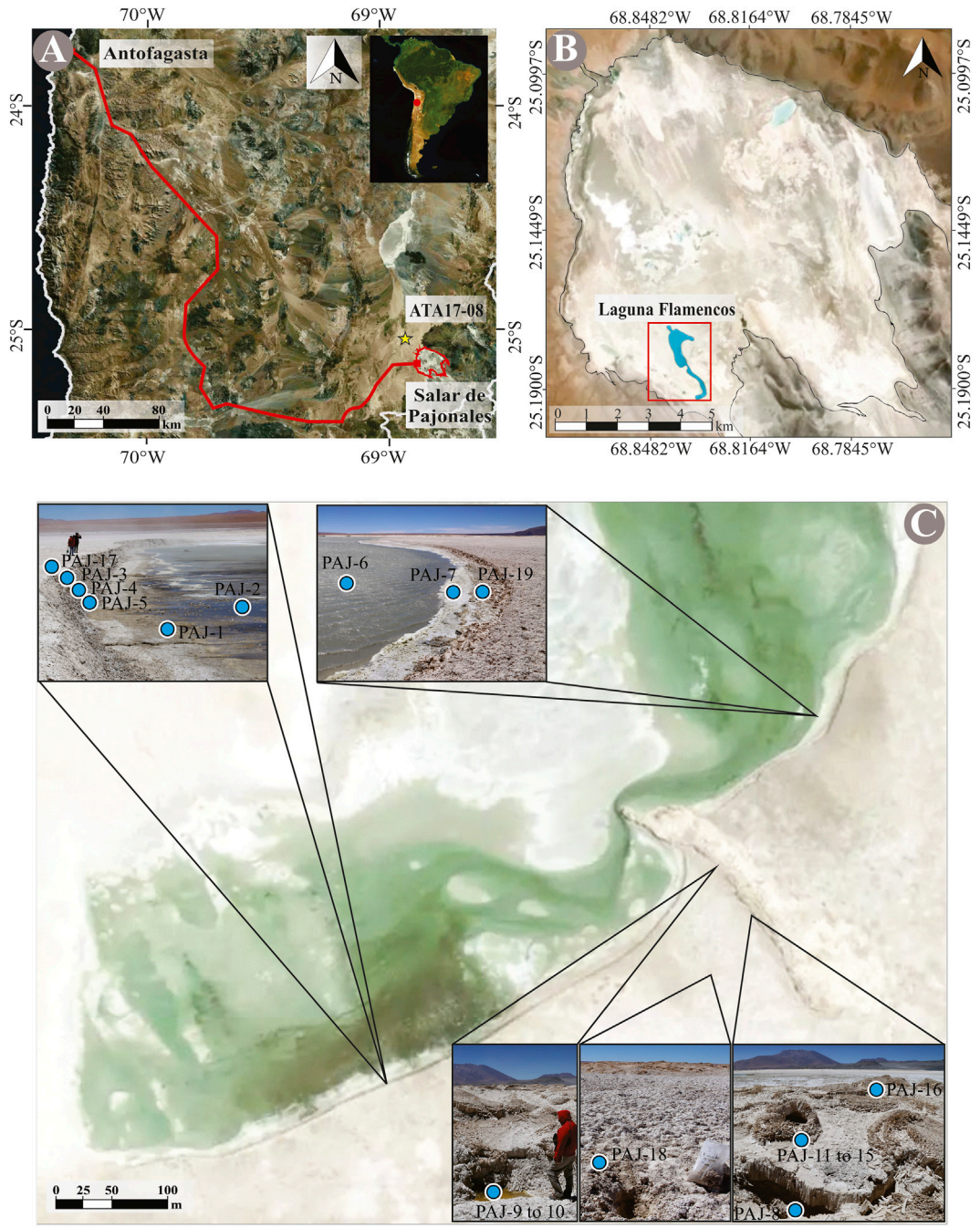

FIGURE 1
(A) Google satellite image showing the location of the Salar de Pajonales (star symbol) and the meteorological station ATA17-08 (red route), located approximately 20 km from the salt flat, in the Antofagasta Region, northern Chile, South America. This station was used as a local climatic reference for the study. **(B)** Terrace near Flamencos Lagoon, an oligohaline peripheral lagoon situated in the southeastern part of the salt flat. **(C)** Overview of the study area highlighting the collected samples, including unconsolidated sediments, stromatolites, and crusts.

laboratory to investigate biosignature formation, preservation, and microbial resilience, with implications for understanding analogs of early Earth and Martian environments (Hinman et al., 2017).

Given this geological and mineralogical diversity, we selected the area close to Flamencos Lagoon, located on the southwestern margin of SP, as our study site. This area is of particular interest because it is surrounded by gypsum platforms bearing stromatolitic structures and includes additional gypsum-rich features such as crusts and unconsolidated sediments, offering a representative setting to investigate microbial-mineral interactions in a high-altitude, evaporitic environment.

The astrobiological relevance of gypsum lies in its stability under arid conditions, its optical transparency to photosynthetically active radiation, and its capacity to entomb biomolecules

and microstructures over geological timescales (Warren-Rhodes et al., 2006; Wierzchos et al., 2006). On Mars, gypsum has been extensively detected *via* orbital spectroscopy (Bibring et al., 2005), prompting speculation about ancient habitable niches in Martian sulfate-rich environments (Warren-Rhodes et al., 2006; Wierzchos et al., 2006; Foster et al., 2020). Stromatolites, which may represent putative biosignatures on Mars (Noffke, 2021), serve as valuable analogs for life detection strategies. It has been argued that Martian evaporitic sulfate sequences should be targeted in searches for life signatures because (i) both modern and ancient Earth analogs demonstrate the habitability of gypsum evaporites, (ii) they possess a high biosignature preservation potential, and (iii) these chemical sediments likely formed where liquid water once existed at the surface (Schopf et al., 2012; Allwood et al., 2013).

Here, we investigated microbial endolithic colonization and biosignature preservation within fossilized gypsum stromatolites using a combination of mineralogical, textural, and elemental techniques, as well as high-taxonomic-resolution analysis (i.e., DNA sequencing) and compound-specific isotopic analysis of lipid biomarkers. Considering the complexity of this microbial ecosystem, we compared the taxonomic and functional diversity of these stromatolites with that of other associated crusts and modern deposits of the salar. Notably, we examined the critical role of water content and mineralogical properties of the samples in determining biosignature preservation and colonization patterns in gypsum.

Materials and methods

Climate data

We included climate data recorded over a 4-year period (2017–2020) to assess dry and wet cycles in the region and evaluate the availability of moisture sources for microbial communities. Due to the lack of prior climate data in the area, a meteorological station (ATA17-08) was installed on 11 April 2017. It was located at 24°57′29.8″S, 68°56′3.9″W, at 3,715 m a.s.l., approximately 20 km west of SP (Figure 1A). The station recorded data every 20 min for 4 years. It was equipped with an Em50 data logger, ECHO20 Utility Mobile software, and sensors from Decagon Devices, Inc. (Pullman, WA, United States) to measure air humidity and temperature, wind speed and direction, soil moisture and temperature, and solar radiation. When available, rainfall events (such as the one recorded on 7 June 2017) were cross-verified using data from nearby meteorological stations within a 200-km radius of the study site, as part of the Chilean National Meteorological System.

Further details regarding standards (range and accuracy) and installation were provided in Supplementary Table S2. We calculated annual, monthly, daily, and hourly averages, as well as monthly average maxima and minima, from various sensors using Tableau software version 2020.2 (Seattle, WA). Additionally, we analyzed the wind direction using a wind rose diagram for different months across the 4-year period using WRPLOT View software version 8.0.2 (WRPLOT, 2021) to identify potential sources of moisture-laden air masses and external mineral inputs contributing nutrients to SP. The Aridity Index (United Nations Environment Programme, 1992) was calculated based on evaporation and precipitation data previously reported by Risacher et al. (1999).

Field work and sample collection

From 2016 to 2019, nineteen samples (ranging from 50 to 500 g) were collected during fieldwork in SP (Table 1). These samples include three categories: unconsolidated sediments, crusts, and stromatolites. The term crust is used here to define a crystalline rock usually not laminated, unlike stromatolites, and often forms as a top layer of unconsolidated sediment. Crusts and stromatolites were collected near and within terraces, while unconsolidated sediment samples were taken from depths of 10–50 cm at the borders of Flamencos Lagoon and near ponds at the study site. Unconsolidated samples were collected using sterilized spatulas with 90% ethanol. Consolidated samples, such as stromatolites and crusts, were obtained using hammers and chisels, also sterilized with 90% ethanol. All samples were placed in a sterile polyethylene zip-lock bag, labeled accordingly, and stored in a cool, dark environment until further processing, which was conducted immediately upon return from the field campaign. For molecular and isotopic analyses of lipid biomarkers, the samples were first wrapped in pre-ashed aluminum foil to prevent potential organic contamination from the polyethylene bags. The wrapped samples were then sealed in polyethylene bags and freeze-dried prior to analysis.

Water content analysis

In the laboratory, sample bags were unsealed to immediately measure the gravimetric water content (GWC). Moisture in unconsolidated sediments, stromatolites, and crusts was determined using the GWC method, following Bilskie (2001). Each sample was analyzed in triplicate by placing 10 g of sample into a glass Petri dish, incubating it at 105 °C for 24 h, and then weighing it after the dish was cooled down for 2 h. This process was repeated until a constant value (difference <0.1%) between two successive measurements was achieved (Blazka and Fischer, 2014). Additionally, the water activity (a_w) of all samples was measured *in situ* using the HygroPalm HP23-AW-A portable water activity equipment (Rotronic AG, Bassersdorf, Switzerland).

Mineralogical analysis

Mineralogical composition was determined using X-ray diffraction (XRD). The samples were pulverized and sieved to particles smaller than 20 µm. Analyses were conducted with a Bruker D8 Advance diffractometer (Bruker AXS GmbH, Karlsruhe, Germany) equipped with a graphite-monochromated Cu-Kα radiation source (λ = 1.54051 Å), operating at 30 mA and 40 kV, with a step size of 0.02° in the 2Θ range and a counting time of 2 s per step. The crystalline phases were interpreted and semi-quantified using EVA software (Bruker AXS, Karlsruhe, Germany) with the Power Diffraction File database (PDF-4+2021) from the International Centre for Diffraction Data (ICDD, Newton Square, PA, United States).

10.3389/fspas.2025.1693302

TABLE 1 Overview of soil moisture measured as gravimetric water content (GWC, %) and water activity (a_w, %) together with the location and mineralogical composition (%) of the samples, including unconsolidated sediments (U.S.), stromatolites (St.), and crusts (C.). Note that the subsamples PAJ-11 and PAJ-12 from PAJ-15 are not included in this overview.

ID	GWC (%)	a_w (%)	Sample type	Spot	Latitude	Longitude	Calcite	Gypsum	Anhydrite	Polyhalite	Epsomite	Kieserite	Halite	Sylvite	Goethite	Magnetite	Hematite	Pinnoite	Ezcurrite	Quartz	Cristobalite	Na-Ca feldspars	Phyllosilicates
PAJ-3	98	84	U.S.	Lagoon shore	-25.1927	-68.8323														17		83	
PAJ-7	65	96.2	U.S.	Lagoon shore	-25.1914	-68.8306	6	12	11				6	3			4			6	5	16	33
PAJ-1	58	96.4	U.S.	Lagoon shore	-25.1927	-68.8323		9					2							9	4	58	18
PAJ-5	57	96.2	U.S.	Lagoon shore	-25.1927	-68.8323		7					2					4		7	4	61	15
PAJ-4	55	96.1	U.S.	Lagoon shore	-25.1927	-68.8323							5		9				6	13	17	50	
PAJ-6	85	97	U.S.	Lagoon bottom	-25.1929	-68.8320	5						4							6	4	57	24
PAJ-2	81	96.4	U.S.	Lagoon bottom	-25.1927	-68.8323		10					3							10	5	52	20
PAJ-10	100	96.2	U.S.	Pond shore	-25.1554	-68.8470	2	79			7	4	6			1							
PAJ-9	100	96.2	U.S.	Pond shore	-25.1927	-68.8323		79			10					2						9	
PAJ-8	98	97	U.S.	Pond shore	-25.1922	-68.8308	8	8					5							8	6	43	22
PAJ-16	13	53	St.	Terrace	-25.1922	-68.8304	12	88															
PAJ-15	11	53	St.	Terrace	-25.1923	-68.8306	1	91			6					2							
PAJ-14	10	50	St.	Terrace	-25.1402	-68.7723		90			8					2							
PAJ-13	10	50	St.	Terrace	-25.1402	-68.7723		93			5					2							
PAJ-19	44	86	C.	Salar surface	-25.1929	-68.8320							100										
PAJ-18	19	76	C.	Salar surface	-25.1927	-68.8305		75					16	1		1						7	
PAJ-17	8	39	C.	Salar surface	-25.1927	-68.8323		39		12			48	1									

Petrographic descriptions using thin sections, μXRF, SEM, and Raman

Microscale descriptions of stromatolites included petrographic analysis and elemental distribution using micro X-ray fluorescence spectroscopy (μXRF), as well as field emission scanning electron microscopy coupled with energy-dispersive X-ray spectroscopy (FE-SEM-EDS). First, to describe the morphological and textural features of stromatolites, vertical thin sections were prepared over relatively large (~12 cm^2) areas of three solid samples. To distinguish carbonate minerals such as calcite (stained red) and dolomite (stained blue) within gypsum crystals, sections were stained with potassium ferricyanide and Alizarin Red S, followed by treatment with 5% acetic acid. Thin sections were observed under plane-polarized light (PPL) and cross-polarized light (CPL) using a petrographic microscope (Nikon Eclipse E400POL, Indiana, United States) at the Departamento de Mineralogía y Petrología, Universidad Complutense de Madrid.

Elemental distributions of intact structures were analyzed using a μXRF instrument (Bruker M4 Tornado, Berlin, Germany) operating at 50 kV with a 600 μA beam current under a 20 mbar vacuum. Areas for analysis were selected based on distinct macroscopic textures observed at the top (red box in Figure 4A) and bottom (green box in Figure 4A) of the structures. μXRF spectra of intact samples were also acquired using a Philips PW-1404 spectrometer equipped with an Sc-Mo X-ray tube and a PR-10 scintillation gas detector. Super-Q Manager Geostandard software (CRNS, France) was used as the analytical database for XRF data processing.

FE-SEM–EDS (SU5000, Hitachi, Tokyo, Japan) was used to characterize the morphology of precipitates and cells in subsamples that had undergone an instant immobilization step prior to cell death, using a fixation–dehydration process. This process consisted of fixation with 4% paraformaldehyde on site, using 0.22 μm filtered saline water at room temperature overnight, followed by dehydration through graded ethanol series (20%, 40%, 60%, 80%, 90%, 95%, 98%, and 100%) at 1-h intervals in a laminar flow chamber (ESCO model AC2-6E8 Class II BSC, Singapore). The subsamples were gold-coated using a Desk II model sputter coater (Denton Vacuum LLC, Moorestown, NJ, United States).

Raman spectroscopy was performed on a set of subsamples from the lower part of the stromatolite to verify the nature of the organic matter observed in thin sections. For this purpose, a DXR Raman confocal microscope (Thermo Fisher Scientific), equipped with a 780 nm laser source, was used at the Museo Nacional de Ciencias Naturales (MNCN), Spain. The Raman OMNIC software suite and the RRUFF database (Lafuente et al., 2015) were used to process the spectra obtained.

Cell viability by autofluorescence pigments

Pigmented microbial communities were taken from stromatolitic samples in sections <0.5 cm thick using a scalpel and placed in an objective holder for immediate visualization with an FV1000 confocal laser scanning microscope (CLSM, Olympus IX-81, Tokyo, Japan) equipped with a ×100 Plan-Apochromat oil-immersion objective lens. To visualize fluorescence, samples were illuminated using an HBO 100 W Hg lamp burner (Olympus, Tokyo, Japan) with different filter cube settings, as described below. DAPI-stained samples exhibiting UV fluorescence were observed using a narrow UV filter cube (360–370 nm excitation and 420–460 nm emission).

Following Roldán et al. (2014), the autofluorescence of photosynthetic pigments in phototrophs was considered an indicator of cell viability. Red autofluorescence of photosynthetic pigments (PAF) served as a marker of photosynthetic activity in phototrophs and was observed using a wide green filter cube (520–550 nm excitation and 580 nm long-pass emission). Green autofluorescence, identifying degraded photosynthetic pigments (GAF), was observed using a wide blue filter cube (460–490 nm excitation and 520 nm long-pass emission).

To generate emission spectra of the autofluorescent molecules, the CLSM λ-scan function was used with an argon laser at 458 nm, covering an emission range from 495 to 695 nm with 5 nm spectral sections and 1 nm step intervals to excite PAF and GAF (Roldán et al., 2014). Fluorescence intensity in regions of interest (ROIs) was determined for each sample as the average relative fluorescence intensity (expressed in arbitrary units, a.u.) across the emission bandwidth. A total of 20 ROIs of 1 μm^2 each were analyzed to quantify fluorescence intensity (0–256 a.u.) and emission range (500–690 nm). Identical settings were applied across all acquired images. Seven photosynthetic pigments were identified, as described in Supplementary Table S3. Additionally, cell and diatom morphotypes were described and classified based on previous studies and reference manuals (Castenholz, 2001; Díaz and Maidana, 2005; Madigan et al., 2018).

Lipid extraction and analysis

Lipid biomarkers were analyzed in eight samples: two stromatolites (PAJ-15, PAJ-16), two crusts (PAJ-18, PAJ-19), and four unconsolidated sediments from the lagoon (PAJ-1, PAJ-2) and ponds (PAJ-9, PAJ-8; Figure 1C). Approximately 50 g of each freeze-dried sample was extracted with a mixture of dichloromethane and methanol (3:1, v/v) using a Soxhlet apparatus for 24 h. Prior to extraction, internal standards were added for hydrocarbons (tetracosane-D_{50}), fatty acids (myristic acid-D_{27}), and alcohols (2-hexadecanol). The total lipid extract was concentrated, cleaned of elemental sulfur, and separated into three polarity fractions: apolar (hydrocarbons), polar (alcohols), and acidic (fatty acids; Sanchez-Garcia et al., 2020). The three lipid fractions were analyzed by gas chromatography-mass spectrometry (GC–MS) using an Agilent 6850 GC system coupled to a 5975 VL MSD with a triple-axis detector (Agilent Technologies, Wokingham, United Kingdom).

Prior to analysis, both the acidic and polar fractions were derivatized with BF_3 in methanol and N,O-bis(trimethylsilyl) trifluoroacetamide (BSTFA), respectively. GC-MS was operated under electron ionization at 70 eV, acquiring full-scan mass spectra (m/z 50–650). The analytes were injected (1 μL) and separated on an HP-5MS column (30 m × 0.25 mm i. d. x 0.25 μm film thickness) with helium as the carrier gas at a flow rate of 1.1 $mL{\cdot}min^{-1}$. Detailed temperature ramps and operating conditions are provided in Sanchez-Garcia et al. (2018).

Compound identification was based on mass spectral comparison with reference materials (C_{10}–C_{40} *n*-alkanes, C_8–C_{24} *n*-fatty acid methyl esters, and isoprenoids) and the NIST mass spectral database. Quantification was performed using external calibration curves of *n*-alkanes (C_{10}–C_{40}), *n*-fatty acid methyl esters or FAMEs (C_8–C_{24}), and *n*-alkanols (C_{14}, C_{18}, and C_{20}), all supplied by Sigma-Aldrich. The recovery of internal standards averaged 75% ± 16%.

In this study, a range of lipid biomarkers was used to infer the presence and function of different microbial groups. Sterols were used as indicators of triterpenoids involved in regulating cell membrane rigidity in eukaryotes (Volkman, 1986). *Iso*- and *anteiso*-branched fatty acids served as key indicators of bacterial presence (Kaneda, 1991), mostly sulfate-reducing bacteria (Taylor and Parkes, 1983; Jiang et al., 2012). Crocetane and dihydrophytol, two isoprenoid hydrocarbons, served as key biomarkers of archaeal biomass (Robson and Rowland, 1993; Carrizo et al., 2022). In addition, phytol, the esterifying alcohol of *chlorophyll a,* was used as a biomarker for photoautotrophs (Didyk et al., 1978). Cyanobacterial biomarkers included monomethylheptadecane, unsaturated alkanes, and unsaturated fatty acids (Shiea et al., 1990; Rontani and Volkman, 2005; Coates et al., 2014). Finally, brassicasterol, an eukaryotic biomarker specific to diatoms, was also detected (Volkman et al., 1998).

Compound-specific isotopic analysis of lipid biomarkers

The carbon isotopic composition of individual lipid compounds was determined by GC-MS (Trace GC 1310 Ultra and ISQ MS, Thermo Scientific, Waltham, MA, United States) coupled to Isotope-Ratio Mass Spectrometry (IRMS) using a MAT 253 instrument (Thermo Fisher Scientific, Waltham, MA, United States). For GC analysis, the oven temperature was programmed to increase gradually from 70 to 130 °C at 20 °C·min^{-1}, and then to 300 °C at 10 °C·min^{-1} (held for 15 min). The IRMS analysis was performed under the following conditions: electron ionization at 100 eV; Faraday cup collectors for *m/z* 44, 45, and 46; and a CuO/NiO combustion interface at 1,000 °C. Samples were injected into a PTV injector in splitless mode, with an inlet temperature of 50 °C, followed by heating to 320 °C at 2.5 °C·s^{-1} (held for 2.5 min). Helium was used as the carrier gas at a constant flow rate of 1.1 mL·min^{-1}.

The isotopic values of the individual lipids separated by GC were calculated using CO_2 spikes of known isotopic composition, introduced directly into the MS source three times at the beginning and end of each run. To ensure the accuracy of $\delta^{13}C$ measurements obtained by GC-IRMS, reference mixtures of *n*-alkanes (A6) and *n*-FAMEs (F8; Indiana University, United States) with known isotopic compositions were used. The $\delta^{13}C$ data for individual carboxylic acids were calculated from the resulting FAME values by correcting for the one carbon atom added during methanolysis (Abrajano et al., 1994). Similarly, $\delta^{13}C$ values for trimethylsilyl derivatives in the polar fraction were corrected for the three carbon atoms added during derivatization.

To assess potential microbial carbon fixation pathways, $\delta^{13}C$ values of individual fatty acids were interpreted in the context of known isotopic patterns associated with the Calvin–Benson–Bassham (CBB) cycle, the reverse tricarboxylic acid (rTCA) cycle, the 3-hydroxypropionate (3HP) bicycle, and the 3HP/4-hydroxybutyrate and dicarboxylate/4-hydroxybutyrate (3HP/4HB and DC/4HB) pathways (Preuß et al., 1989; van der Meer et al., 2000; Hayes, 2001).

Bulk isotopic analysis

The stable isotope composition of organic carbon ($\delta^{13}C$) and total nitrogen ($\delta^{15}N$) was measured on bulk freeze-dried SP samples by IRMS using a MAT 253 instrument (Thermo Fisher Scientific, Waltham, MA, United States), following analytical methods from the U.S. Geological Survey (Révész et al., 2012) as described in Carrizo et al. (2019). Briefly, ~300 mg of dry sample were decarbonated with HCl (37%). After equilibration for 24 h and pH adjustment to neutral values using ultrapure water, the residue was dried at 50 °C in an oven for 72 h and subsequently analyzed by IRMS. Ratios of the heavy to light stable isotopes of $\delta^{15}N$ and $\delta^{13}C$ were reported in the standard per mil (‰) notation using three certified standards (USGS41, IAEA-600, and USGS40), with an analytical precision of ±0.1‰. In parallel with the stable isotope analysis, total organic carbon (TOC) and total nitrogen (TN) contents were determined using an elemental analyzer (HT Flash, Thermo Fisher Scientific, Waltham, MA, United States) and reported as percentages relative to dry weight.

Total DNA extraction

For microbial cell separation from organic gels and minerals, a combination of mechanical and chemical methods was modified from Demergasso et al. (2008) and Bey et al. (2011). High-molecular-weight DNA was extracted from 50 g of wet organic gel, which was blended three times in 100 mL of sterile salt solution (PBS buffer 1× and Tween 20 at 10% v/v) using an Ultramax blender (A3D, China) at 18,000 rpm for 1 min with intermittent cooling for 1 min at −20 °C. To enhance cell removal, the final blended slurry was shaken at 120 rpm for 30 min, and the supernatant was centrifuged at 3,500 rpm. Microorganisms were collected by filtration through a 0.22 µm nitrocellulose Millipore filter (Merck-Millipore, Germany), and the filters were washed with 500 mL of sterile PBS solution (pH 7.0, adjusted for salinity) to ensure the removal of most salts and organic residues.

The filters containing cells were stored at −20 °C in 1 mL hypertonic lysis buffer (50 mM Tris–HCl pH 8.3; 40 mM EDTA; and 0.75 M sucrose) until further processing. For cell lysis, the filters were frozen and thawed three times at −80 °C and 65 °C for 5 min each step, and then incubated with lysozyme (40 mg·L^{-1}) at 37 °C for 1 h and proteinase K (20 mg·mL^{-1}) at 55 °C for 45 min. Genomic DNA was extracted using a High Pure Template Preparation Kit (Qiagen, United States).

Purified DNA from all the samples was pooled in equimolar ratios to a final concentration of approximately 100 ng·µL^{-1}. DNA integrity and quantification were assessed by agarose

gel electrophoresis (1%, w/v), and DNA/RNA (260/230) and DNA/protein (260/280) ratios were determined using UV–visible spectrophotometry (Nanodrop NP1000, Thermo, Germany). Although DNA extraction was attempted for samples PAJ-11 to PAJ-13, yields were insufficient because these were subsamples of larger stromatolite specimens.

Diversity through 16S rRNA sequencing

Sequencing was performed according to the manufacturer's guidelines (MR DNA, 2019). The hypervariable regions of the 16S rRNA gene, V1–V3 for Bacteria and V3–V4 for Archaea, were amplified from each sample using the primers listed in Supplementary Table S4. The resulting libraries were sequenced on an Illumina MiSeq platform.

Taxonomic and phylogenetic analysis

Demultiplexed FASTQ files from 18 bacterial and 16 archaeal samples were first trimmed to remove their primers using Cutadapt version 1.8.1 (Martin, 2011). Subsequently, bacterial and archaeal sequence sets were independently cleaned, filtered, trimmed, dereplicated, merged, and checked for chimeras using a modified Divisive Amplicon Denoising Algorithm 2 (DADA2) pipeline version 1.20.0 (Callahan et al., 2016) in R software version 4.1.1 (R Core Team, 2024), which corrects and clusters reads into amplicon sequence variants (ASVs). Sequence quality thresholds were defined by trimming reads to 250 bp for both forward and reverse sequences, retaining those with a PHRED quality score above 30. In most samples, paired-end reads with consistent overlap were merged using the standard DADA2 workflow. Representative reads were taxonomically assigned against the SILVA database, release 138 (Quast et al., 2013). In Phyloseq version 1.36.0 (McMurdie and Holmes, 2013), all sequences underwent quality control following these steps: (a) removal of taxa represented by a single read, (b) exclusion of taxa with less than 0.005% mean relative abundance across all samples, (c) elimination of samples with fewer than 1,000 reads, and (d) rarefaction of the dataset to the smallest sample size (1,613 and 2,818 reads for bacterial and archaeal ASVs, respectively) using the *rarefy_even_depth* function.

The resulting ASV tables, taxonomy table, and associated categorical (Supplementary Table S5) and numerical variables (e.g., mineral composition, GWC, and a_w; Table 1) were integrated and managed using the PRIMER 6 software package (Clarke and Gorley, 2006).

For phylogenetic analysis, Cyanobacteria ASVs from this study, along with 37 closely related reference sequences identified *via* BLASTn and retrieved from the GenBank database, were compiled. Multiple sequence alignment was performed using ClustalW (Thompson et al., 2002), followed by manual removal of poorly aligned regions. A maximum-likelihood phylogenetic tree was constructed using MEGA11 (Tamura et al., 2021) with the GTR substitution model and 1,000 bootstrap replicates.

Statistical analysis

Relative abundances of ASVs were calculated to characterize microbial community composition at the phylum and genus levels. Additionally, bacterial and archaeal genera (with >1% relative abundance in at least one sample) from unconsolidated sediment, crust, and stromatolite samples were analyzed in PRIMER 6 (Clarke and Gorley, 2006). The distribution of genera by sample type was visualized using a Venn diagram generated with the online tool described by Oliveros (2007–2015).

Alpha diversity was calculated using the Shannon index (H', an entropy-based measure of ASV abundance), Pielou's evenness index, Simpson's index ($1-\lambda'$, dominance measure), and Margalef's richness index, all computed in PRIMER 6 (Clarke and Gorley, 2006). Shannon index values were correlated with GWC and a_w using Pearson correlation coefficients (r >0.5).

For statistical analyses, a fourth-root transformation was applied to homogenize ASV abundances and reduce the influence of dominant taxa. A resemblance (similarity) matrix of the transformed data was constructed using the Bray–Curtis similarity measure. Hierarchical clustering (CLUSTER method) was then applied to generate a dendrogram, and similarity profiles were tested with SIMPROF using 999 permutations. Environmental variables, including GWC, a_w, and mineralogical composition, were analyzed in relation to the bacterial and archaeal α-diversity using Pearson correlation, coefficient of determination (r^2), and p-value.

The similarity matrix of the microbial community was further examined using Principal Coordinates Analysis (PCoA). Metadata variables (GWC, a_w, mineralogical composition, and dominant bacterial and archaeal phyla) were correlated using Pearson coefficients (r >0.5). This approach allowed us to calculate and visualize the relationships between the variables and the ordination axes, which were displayed as overlaid vectors on the PCoA plots. Finally, a permutational multivariate analysis of variance (PERMANOVA; Anderson et al., 2008) with 9,999 permutations was conducted to test the significance of multivariate factors listed in Supplementary Table S5.

Data availability

The bacterial and archaeal sequence data have been deposited in the DNA Data Bank of Japan (DDBJ) under BioProject PRJDB19570, with accession numbers DRR622817–DRR622830 and DRR622831–DRR622842, respectively. In addition, BioSample metadata for the bacterial and archaeal sequence data are available in the DDBJ BioSample database under accession numbers SAMD00845097–SAMD00845109 and SAMD00845872–SAMD00845882, respectively.

Results

Climate characteristics of Salar de Pajonales

Daily air temperatures ranged from −16 °C to 15 °C (Figure 2A), with extreme values reaching −23 °C during the

10.3389/fspas.2025.1693302

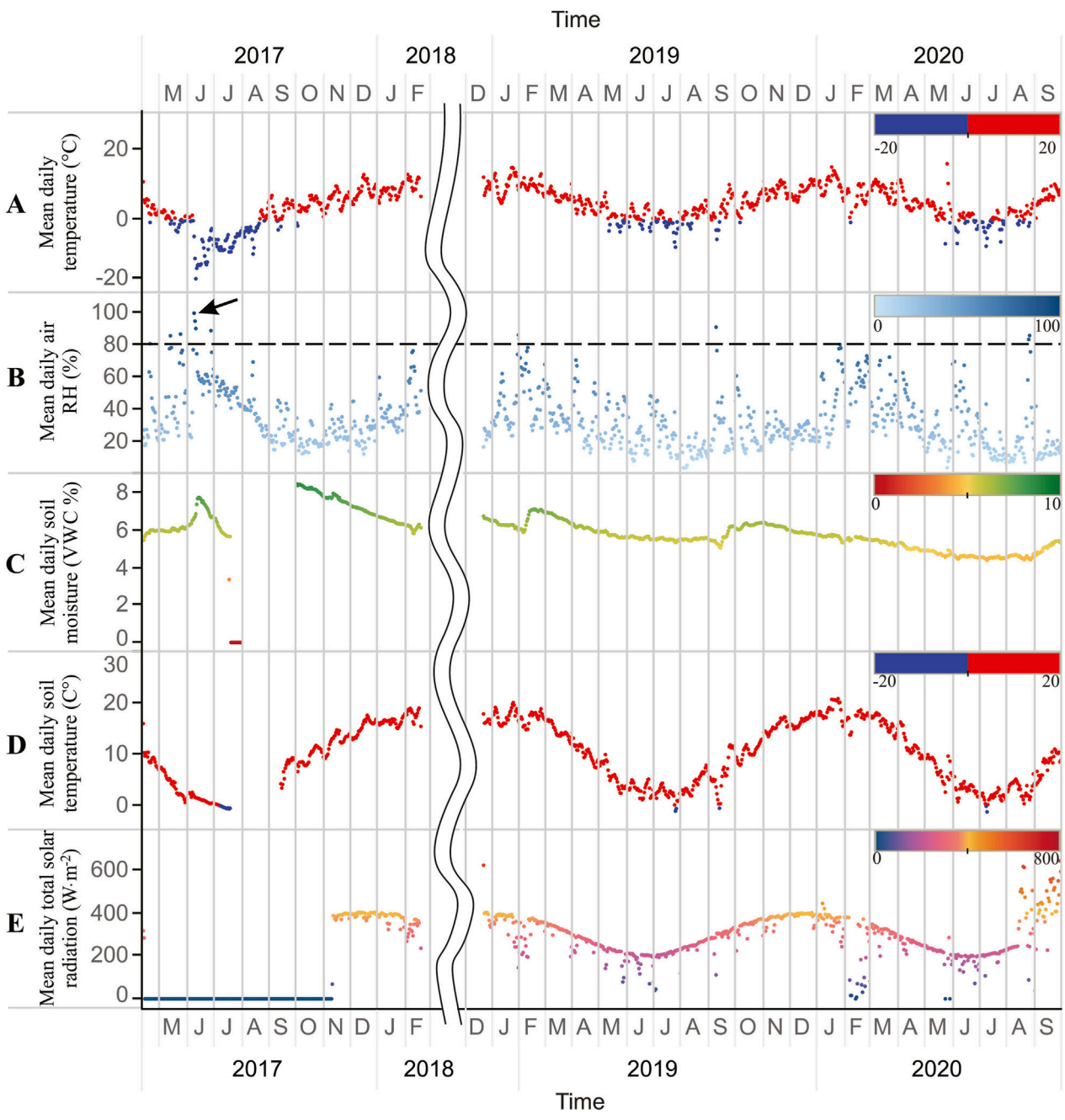

FIGURE 2
Climate conditions recorded between April 2017 and September 2020 at the meteorological station near SP, showing mean daily values of **(A)** air temperature, **(B)** relative humidity (RH%), **(C)** soil moisture (volumetric water content, VWC%), **(D)** soil temperature, and **(E)** total solar radiation. In panel B, the dashed horizontal line marks 80% relative humidity, and the black arrow highlights a period reaching saturation (100% RH) on 7 June 2017.

austral winter and up to 26 °C in summer, and an average of 4 °C (Supplementary Table S6). The annual average wind speed was 5 $m{\cdot}s^{-1}$, with a maximum of 31 $m{\cdot}s^{-1}$ (Supplementary Table S6). Wind rose diagrams (Supplementary Figure S1) indicated that winds predominantly blew from the southeast to the northwest for significant periods throughout the day. During each season, nighttime winds typically came from the southeast at lower speeds (hourly medians = 2.6–4.3 $m{\cdot}s^{-1}$ in each season; Supplementary Figure S1B). Shortly after sunrise, wind direction shifted from southeasterly to northwesterly, with increased speeds ranging from about 5.7 to as high as 11 $m{\cdot}s^{-1}$ (Supplementary Figure S1B). The highest wind speeds occurred between 14:00 and 19:00 h (Supplementary Figures S2A,B).

The daily average of air RH was 33% (Supplementary Table S6), with a peak of 100% on 7 June 2017, and the lowest values recorded in winter, reaching a mean of just 13% RH in August 2019 (Figure 2B). The highest RH values generally occurred between 06:00 and 07:00 h, ranging from 40% to 60%

(Supplementary Figure S2B). Soil moisture and temperature showed strong seasonal patterns (Figures 2C,D), with maximum soil VWC reaching up to 8.5% at 7.9 °C and a minimum of 0% at −6 °C (Supplementary Table S6).

Solar radiation levels in Salar de Pajonales ranged from 183 to 446 $W{\cdot}m^{-2}$, with a daily average of approximately 304 $W{\cdot}m^{-2}$ (Figure 2E). The highest recorded value reached 1,317 $W{\cdot}m^{-2}$ on 29 January 2020, at 13:20 h (Supplementary Figure S2D and Supplementary Table S6). Based on these measurements, the aridity index was calculated to range between 0.06 and 0.1, classifying the climate of Salar de Pajonales as continental arid.

From June 6 to 10 June 2017, an extreme climatic event was recorded (Supplementary Figure S3), marked by a sharp temperature drop from 0 °C to −23 °C and a rise in RH from 28% to 100%, which remained elevated (90%–100%) throughout the period. Soil VWC increased from 6.6% to 7.8%, while ground temperature declined from 2.3 °C to 1.4 °C. Additionally, three other instances of RH exceeding 80% were recorded: 31 January 2019 (~83%), 8 September 2019 (~90%), and 26 August 2020 (~85%).

Microbial ecosystems in Flamencos Lagoon

We studied microbial communities within stromatolites located on the terrace, as well as in nearby unconsolidated sediments and crusts, in the southwestern sector of Salar de Pajonales, near Laguna Flamencos (~579,280 m^2; Figure 1B). This lagoon is fed by springs emerging along its margins, which in some areas form small ponds or shallow pools that are superficially disconnected from the main water body classified as oligohaline waters (18–48 $g{\cdot}L^{-1}$ NaCl; Risacher et al., 1999).

The collected unconsolidated samples included brownish sediments (PAJ-1, PAJ-3 to PAJ-5, PAJ-7; Figure 1C) and black sediments (PAJ-2, PAJ-6; Figure 1C) retrieved from the lagoon bottom, as well as precipitates (PAJ-8 to PAJ-10; Figure 1C) obtained from evaporitic ponds adjacent to the lagoon. The consolidated samples comprised selenitic crystals (PAJ-11 to PAJ-13; Figure 1C) extracted from former stromatolites (PAJ-15 to PAJ-16; Figure 1C) found on meter-scale terraces now subject to erosion, and evaporitic crusts (PAJ-17 to PAJ-19; Figure 1C) occurring over the salar surface between the lagoon and the terraces. These terraces, composed of ancient gypsum deposits, are geomorphological features formed by past lake-level fluctuations or evaporitic surface retreat and now lie roughly 5 m above the present lagoon level.

Based on macroscale observations, samples were categorized by both location and sample type: unconsolidated sediments from the lagoon and ponds, stromatolites from terraces, and surface crusts from the salt flat (Table 1). The unconsolidated sediments consisted of thin layers of green or red biofilms embedded within gray and brown precipitates, found near (Supplementary Figures S4A,B,D,E) and approximately 1 m away from the lagoon shoreline (Supplementary Figures S4F–H). In contrast, unconsolidated sediments in evaporitic ponds exhibited greenish biofilms that agglutinated white precipitates (Supplementary Figure S4C).

On the eastern side of the lagoon, the terrace hosted meter-scale domical stromatolites composed of gypsum crystals. These stromatolites displayed well-defined domical morphologies (Supplementary Figures S5A,E), characterized by vertically oriented, radially arranged selenitic gypsum crystals reaching up to 15 cm in length (Supplementary Figures S5B,F). Beneath these crystals, centimeter-thick laminated structures formed the basal portion of the stromatolites, enclosing a central hollow cavity up to 10 cm wide (Supplementary Figures S5E,H). In the upper part of the domes, the gypsum crystals showed signs of dissolution, resulting in irregular terminations and suggesting interruptions in crystal growth. Just beneath the crystal surfaces, a network of millimeter-sized corrosion pits was observed, colonized by green and pink pigmented microbial communities organized in distinct laminations—indicative of active endolithic colonization (Supplementary Figures S5C,G).

Between the lagoon and the terrace, grayish-white evaporitic crusts covered the salt flat surface, showing irregular (e.g., cerebroid) and globular morphologies likely shaped by subsurface gas accumulation (Supplementary Figures S6A–C).

Moisture content and mineralogical composition

X-ray diffraction and water content analyses of 17 samples (Table 1; Supplementary Table S7) revealed clear differences in mineralogical composition and moisture content among unconsolidated sediments, stromatolites, and crusts. Unconsolidated sediments showed high moisture values (55%–100% GWC; 84.0%–96.4% aw) and were mainly composed of Na–Ca feldspars (54%), phyllosilicates (16%), quartz (10%), and cristobalite (6%), with minor phases (≤4%) such as gypsum, halite, sylvite, and calcite (Supplementary Table S7). Unconsolidated sediments from ponds were more variable, ranging from gypsum-rich deposits (up to 53%, with minor epsomite, halite, calcite, and kieserite) to more detrital assemblages dominated by feldspars (17%), phyllosilicates (7%), quartz (3%), and cristobalite (2%). In contrast, stromatolites exhibited lower moisture (8%–44% GWC; 39%–86% a_w) and consisted mostly of gypsum (91%) with minor epsomite (5%) and calcite (3%), whereas crusts displayed very low moisture (10%–13% GWC; 50%–53% a_w) and were characterized by halite (55%) and gypsum (38%), with minor polyhalite (4%) and sylvite (1%).

Microscale descriptions of stromatolites

Petrographic thin sections analysis (Figure 3) was performed on stromatolites and revealed a domical microstructure with two distinct parts. The lower part displayed a domical shape with internal laminar intercalations of bright crystalline laminae and darker, porous, organic-matter-enriched bands (Figure 3A; Supplementary Figure S7). The darker bands were associated with gypsum crystals showing signs of dissolution and the presence of gas bubbles like remains (Figure 3B). In this part, 100–200 µm spherulitic gypsum (Figure 3C) and fluid inclusions following exfoliation and growth planes within the gypsum crystals were observed (Figure 3D). In addition, diatom frustules resembling *Amphora* sp. (Figure 3E), together with filamentous cells (Figure 3F), were observed entombed within gypsum crystals

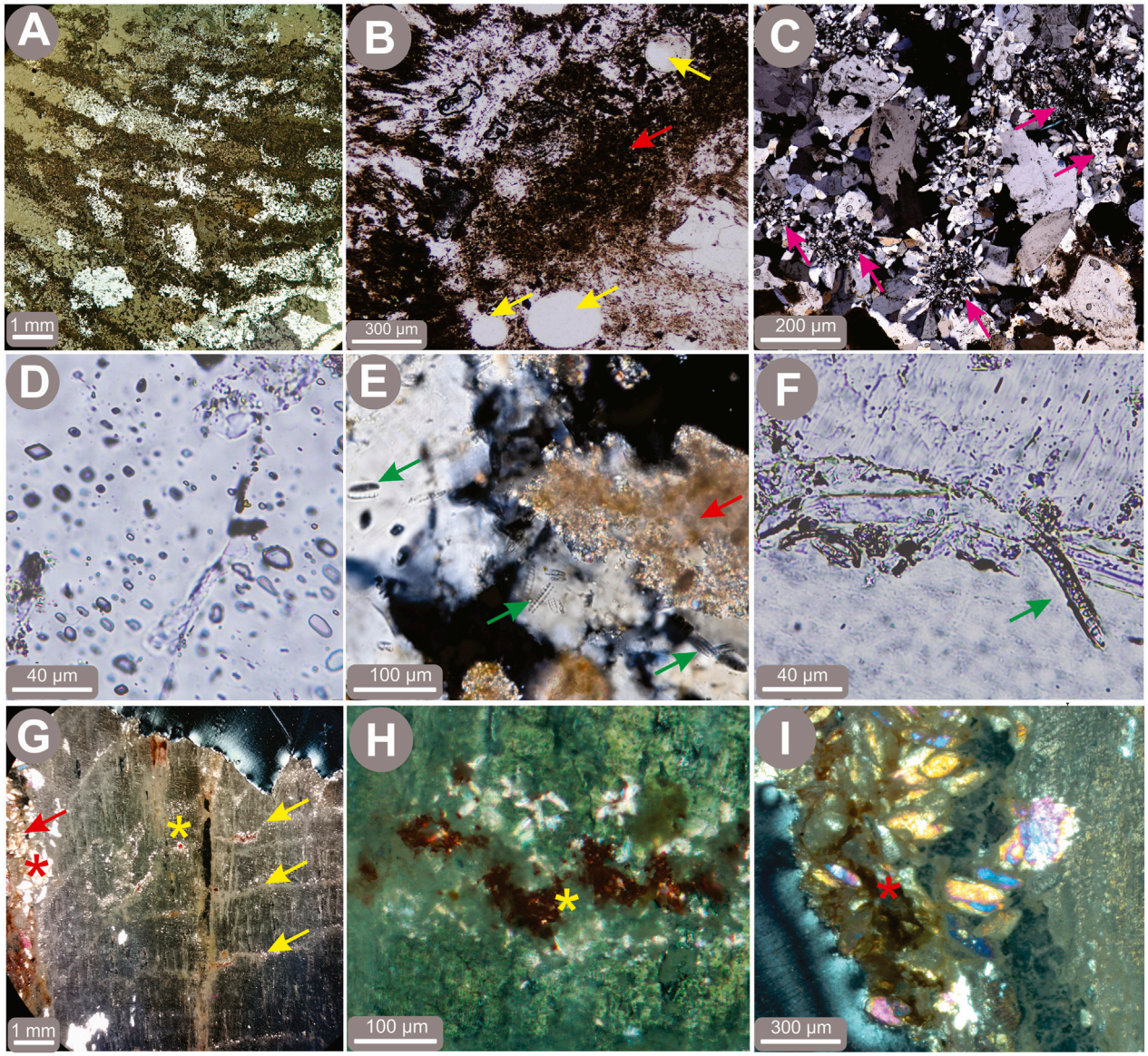

FIGURE 3
Transmitted- and polarized-light photomicrographs of the lower **(A–F)** and upper **(G–I)** parts of stromatolitic sample PAJ-15. **(A)** Low-magnification overview showing alternating bright crystalline laminae and darker, porous, organic-matter-enriched bands following the exfoliation and growth planes of gypsum crystals. **(B)** Vug-like structures resembling gas bubbles (yellow arrows) embedded within organic matter (red arrows). **(C)** Radially oriented spherulitic aggregates of gypsum crystals (pink arrows). **(D)** Remnants of fluid inclusions along exfoliation and growth planes. **(E)** Diatom frustules (green arrows) resembling *Amphora* sp. within gypsum crystals embedded in organic matter (red arrow). **(F)** Filamentous microorganisms enclosed within gypsum crystals (green arrow). **(G)** Low-magnification view highlighting porosity in both the interior (yellow arrows) and exterior (red arrows) regions of gypsum crystals. **(H, I)** Calcite precipitates (stained red) filling these porosities along growth and exfoliation surfaces (yellow asterisks in **(G, H)**) and along vertical cleavage planes (red asterisk in **(G, I)**).

embedded in organic matter. the upper part or microstructure showed gypsum crystals exhibiting both external and internal signs of dissolution (Figures 3G–I). Calcite precipitates were observed filling porosities within exfoliation and growth planes (Figure 3H), as well as within vertical cleavage planes (Figure 3I).

In stromatolites, µXRF analyses revealed distinct textural and fine-scale mineralogical features (Figures 4A–D). The lower section exhibited micro-layering (Figures 4E–H), while the upper section displayed a fishtail texture (Figures 4I–L). Both sections consisted of Ca–S-bearing and Fe–Si-bearing minerals (Figures 4F,G,J,K), with a strong sulfur signal (Figures 4D,H,L). These two zones exhibited contrasting mineral-organic associations and localized iron enrichment. Although Fe and Si exhibited relatively intense X-ray signals, their spatial distribution varied. In the lower section, Si was detected in horizontal layers (Figure 4F), likely associated with diatom remains, whereas in the upper section, it was aligned along exfoliation and growth planes of gypsum crystals (Figure 4J). Conversely, Fe was locally enriched in intercalated Si-bearing layers at the base of the structure (Figure 4G) and also appeared as discrete spots (Figure 4K) along the exfoliation and growth planes

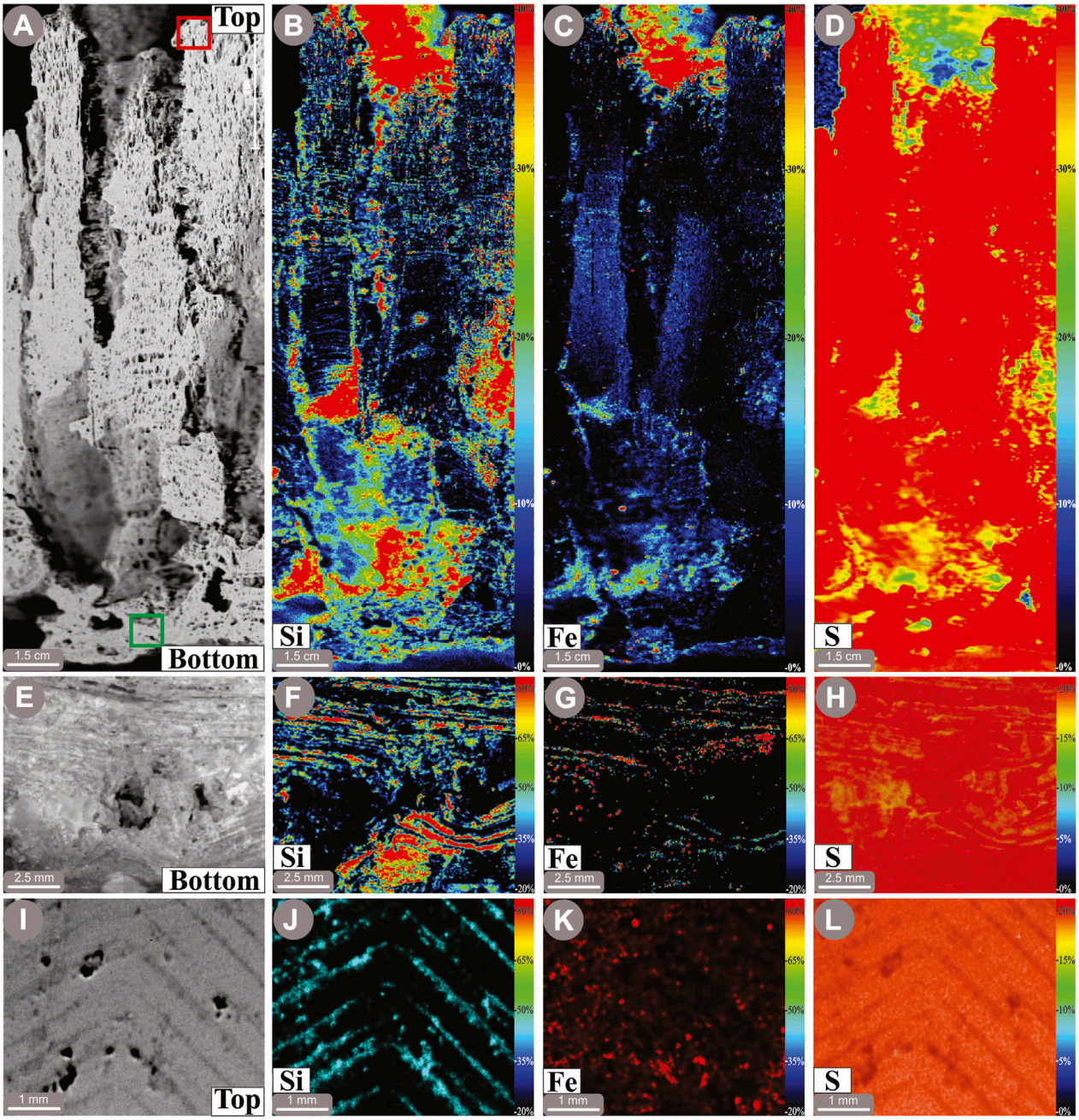

FIGURE 4
μXRF maps of the entire **(A–D)**, bottom **(E–H)**, and top **(I–L)** sections of the stromatolitic structure in sample PAJ-15, illustrating the distribution of iron (Fe), silicon (Si), and sulfur (S). The color scale indicates background intensity with blue representing values below the detection limit and red indicating the maximum measured intensity. The map dimensions are 250 μm × 150 μm, and mapping was conducted using incremental steps of 0.5 μm × 0.75 μm.

of gypsum crystals. This pattern highlights the dominance of Fe-Si-rich layers in the lower part of the stromatolite compared to the upper section.

FE-SEM-EDS analyses of stromatolitic textures revealed distinct biosignatures within gypsum crystals in the lower (Figures 5A–D) and upper sections (Figures 5E–I). In the lower part, stromatolitic textures exhibited micrometric intercalations of dark organic layers and bright layers mainly composed of gypsum (Figures 5A,B). Rounded cavities within gypsum crystals, possibly remnants of gas bubbles from microbial activity, were also observed (Figures 5A,B).

Mineral distribution within the gypsum crystal in the lower layers revealed two main observations: (i) a thick, light-gray gypsum layer showing corrosion features, with fissures and cavities filled by darker gray Si-rich aggregates (Figure 5B), and (ii) diatom frustules embedded within cavities of gypsum crystals (Figures 5B,C). Numerous broken and intact diatom frustules,

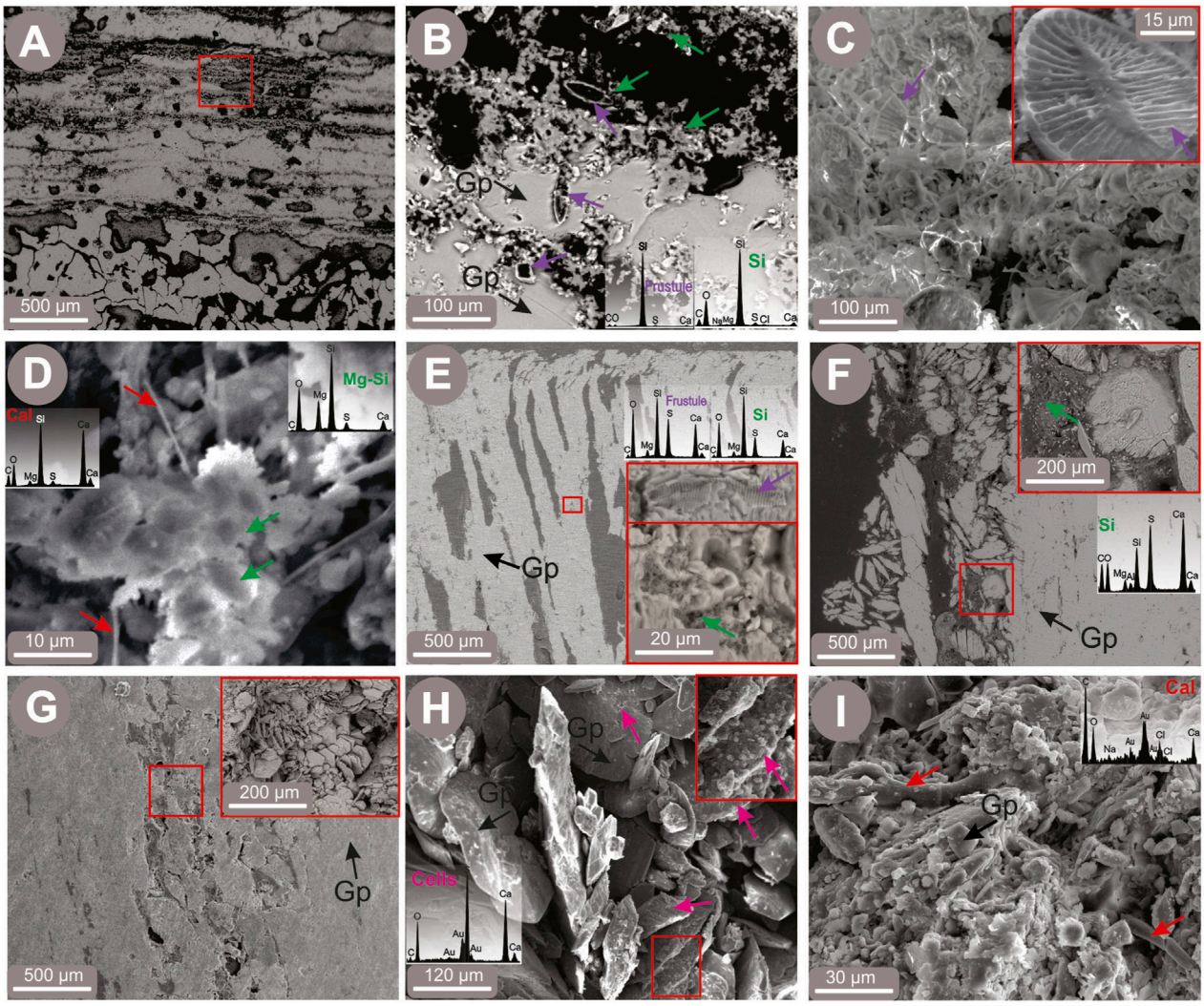

FIGURE 5
SEM-EDS micrographs of thin sections from the lower **(A–D)** and upper **(E–I)** parts of stromatolitic structures (PAJ-11 to PAJ-15) showing evidence for biosignatures inside gypsum (Gp) crystals. **(A)** Lamination with dissolution signs in the lower part of structure. **(B)** Overview of red square in **(A)** showing rounded cavities, diatom frustules (purple arrows), and rounded Si-rich aggregates (green arrows) within dissolved horizontal laminations inside gypsum crystals (black arrows). **(C)** Remnants of diatom frustules belonging to the Bacillariophyceae family. **(D)** Rounded Mg-Si aggregates (green arrows), and filamentous aggregates of calcite (Cal; red arrows). **(E, F)** Dissolution signs on cleavage, exfoliation and growth planes of gypsum crystals in the upper part of structure, including diatom frustules (purple arrow) and rounded Si-rich aggregates (green arrows). **(G, H)** Lenticular-shaped gypsum crystals inside porosities of gypsum crystal at the upper part of structure. **(H, I)** Unicellular (pink arrows in **H**) and filamentous (red arrows in **I**) cyanobacterial cells on lenticular crystals, including calcite (Cal) precipitates on cells. Note: oval, unicellular cyanobacterial cells compatible with the genus *Chroococcidiopsis* sp. and diatom frustules from the Bacillariophyceae family resemble the genera *Amphora* sp. (purple arrows in **B**) and *Surirella Sella* (purple arrows in **C**).

identified as belonging of the family Bacillariophyceae, resembled the genera *Amphora* (Figure 5B) and *Surirella sella* (Figure 5C). Additionally, Si–Mg aggregates with ~5 µm in diameter were observed within the gypsum cavities, along with fibers containing carbon consistent with filamentous cells (Figure 5D).

In the upper part, micrometric dissolution features appeared as dark areas within bright regions of gypsum crystals, showing entombed diatom frustules and Si-rich alveolar textures (Figure 5E). Dissolved cleavage planes were filled with Si-rich aggregates, likely derived from diatom frustules, and subhedral gypsum microcrystals oriented in different directions (Figure 5F). Further observations along exfoliation and growth planes revealed lenticular gypsum crystals up to 100 µm in size (Figures 5G,H), with rounded cells (Figure 5H), possibly belonging to the *Chroococcidiopsis* sp., as well as filamentous cells likely representing *Nodosilinea* sp., both associated with high carbon peaks indicative of calcite precipitates (Figure 5I).

Cell morphotypes in gypsum and their autofluorescence pigment fingerprinting

Confocal laser scanning microscopy (CLSM) revealed three distinct cyanobacterial morphotypes inhabiting the upper gypsum

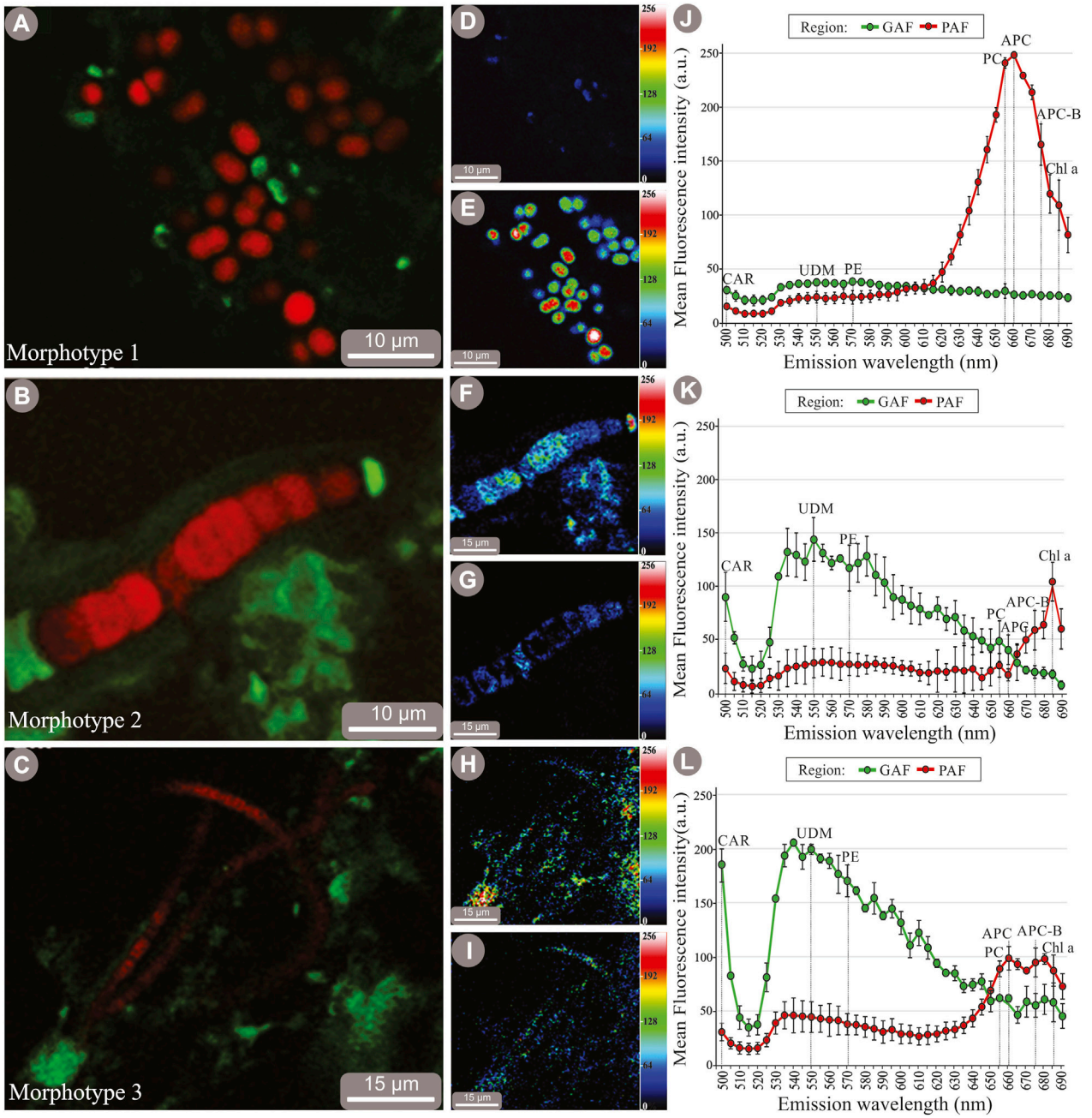

FIGURE 6
Photosynthetic pigments as indicators of cell viability in three morphotypes observed within gypsum crystals in the upper part of stromatolitic structures at the Salar de Pajonales (samples PAJ-11 to PAJ-15), analyzed using fluorescence **(A–C)** and λ-scan **(D–L)** modes of a CLSM. In the fluorescence mode, using specific filters (**A–C**; Supplementary Figure S8), the morphotypes exhibited varying intensities of red autofluorescence due to photosynthetic pigments (PAF) and non-specific autofluorescence resulting from degraded photosynthetic pigments (GAF). Unicellular cells **(A)** displayed an intense PAF signal, while filamentous cells **(B, C)** showed a strong GAF signal. Autofluorescence images obtained through CLSM λ-scan **(D–I)** and the corresponding emission spectra **(J–L)** illustrate the fluorescence intensity (a.u.) as a function of emission wavelength for the three morphotypes. The spectra reveal GAF **(D, F, H)** and PAF **(E, G, I)** signals excited by a 458-nm laser. Notable peaks include 500 nm for carotenoids (CAR), 548 nm for unknown degraded molecules (UDM), 570 nm for phycoerythrin (PE), 657 nm for phycocyanin (PC), 662 nm for allophycocyanin (APC), 675 nm for allophycocyanin-B (APC-B), and 685 nm for *chlorophyll a* (Chl *a*).

layers of the stromatolites (Figure 6; Supplementary Table S8). These included unicellular aggregates (morphotype 1, compatible with *Chroococcidiopsis*; Figure 6A) and two filamentous forms, morphotype 2 (morphologically consistent with *Phormidium;* Figure 6B) and morphotype 3 (tentatively identified as *Nodosilinea*; Figure 6C), which were confined to the pigmented layers and absent in the lower sections.

Autofluorescence imaging showed both green (GAF) and red (PAF) emissions, corresponding to degraded and photosynthetic pigments, respectively. GAF was distributed in a

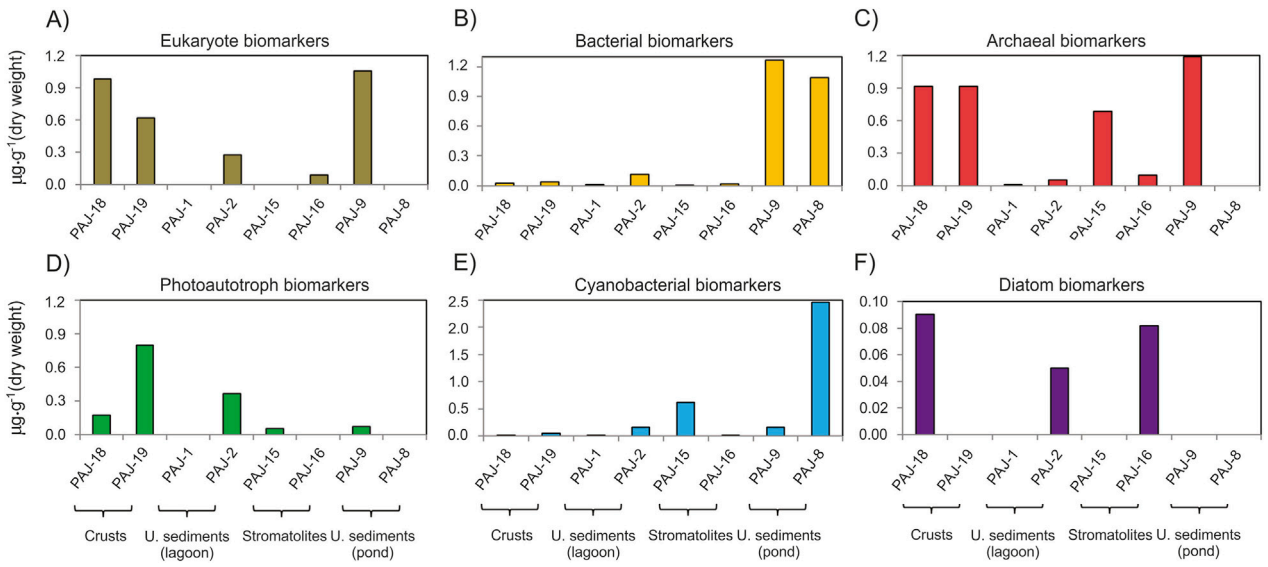

FIGURE 7
Relative abundance of lipid biomarkers assigned to biological groups and sample types from the Salar de Pajonales, including unconsolidated ("U.") sediments from the lagoon (PAJ-1 and PAJ-2), stromatolites (PAJ-15 and PAJ-16), two unconsolidated sediments from ponds (PAJ-8 and PAJ-9), and crusts composed mainly of gypsum (PAJ-18) and halite (PAJ-19). The concentration of lipid compounds (µg·g^{-1} dry weight) is attributed to: **(A)** eukaryotes (sum of sterols such as cholesterol, stigmastanol, and β-sitosterol), **(B)** bacteria (sum of branched fatty acids with *iso* and *anteiso* configurations), **(C)** archaea (sum of crocetane and dihydrophytol), **(D)** photoautotrophs (phytol), **(E)** cyanobacteria (sum of 7-methylheptadecane, 8-heptadecene, 9-nonadecene, 9-hexadecenoic acid, 9-octadecenoic acid, and 11-octadecenoic acid), and **(F)** diatoms (brassicasterol).

heterogeneous pattern within the cell cytoplasm (Figures 6D,F,H) and in the outer mucilaginous envelopes, while PAF showed a homogeneous distribution across the cell cytoplasm (Figure 6E; Supplementary Figure S8). These cyanobacteria were accompanied by smaller bacterial and archaeal cells distributed among the gypsum crystals and stained with DAPI (Supplementary Figure S8).

Spectral fingerprints indicated differences in pigment composition. Morphotype 1 was dominated by phycocyanin, allophycocyanin, and *chlorophyll a* (Figure 6J), whereas the filamentous morphotypes exhibited stronger signals of carotenoid, phycoerythrin, and unknown degraded molecules (Figures 6K,L). Together, these autofluorescence profiles demonstrate the functional and structural stratification of phototrophic communities within gypsum stromatolites.

Lipid biomarkers

Lipid biomarker analyses revealed diagnostic compounds representing eukaryotes, bacteria, archaea, cyanobacteria, photoautotrophs, and diatoms across gypsum-rich habitats in the Salar de Pajonales (Supplementary Table S9; Figure 7). Eukaryotic sterols such as cholesterol, stigmastanol, and β-sitosterol were most abundant in crusts and unconsolidated sediments, ranging from 0.08 to 1.1 µg g^{-1} of sample dry weight (dw; Figure 7A). Bacterial *iso*- and *anteiso*-branched fatty acids occurred ubiquitously in all SP samples, with the highest concentrations in pond-edge sediments (Figure 7B). Archaeal lipids, including crocetane and dihydrophytol, were detected in nearly all samples, except in the unconsolidated sediment PAJ-8 (Figure 7C).

Photoautotrophic signatures (e.g., phytol) were present in crusts, stromatolites, and sediments, consistent with active phototrophic communities (Figure 7D). Cyanobacterial biomarkers, such as monomethylheptadecane, unsaturated alkanes (8-heptadecene, 9-nonadecene), and unsaturated fatty acids (16:1ω7, 18:1ω7, 18:1ω), were abundant across all sites, particularly within pigmented stromatolite layers and unconsolidated sediments near ponds (Figure 7E). The diatom marker brassicasterol was restricted to stromatolite PAJ-16, crust PAJ-18, and unconsolidated sediment PAJ-2 (Figure 7F).

Based on the organic extract profiles, lipid compounds characteristic of phototrophic groups predominated over those from other sources. The highest cyanobacterial lipid concentrations were found in stromatolite PAJ-15 (Figure 7E), which also showed the greatest cyanobacterial abundance according to microscopy (Figure 6) and 16S rRNA gene sequencing (Figure 9C). Similarly, lipid signals of diatoms in PAJ-16 and PAJ-18 corresponded with the presence of diatom-related DNA. In addition, the well-preserved state of lipids, particularly in the crust samples, was suggested by the high proportion of saturated relative to unsaturated fatty acids (data not shown).

Stable-carbon isotopic composition of the lipid biomarkers

Compound-specific isotopic analysis of the identified fatty acids returned $\delta^{13}C$ values ranging from −34.5 to −8.6‰ (Figure 8). These values are compatible with synthetic pathways such as the CBB Cycle ($\delta^{13}C$ of ca. −19 to −34‰), the rTCA pathway ($\delta^{13}C$

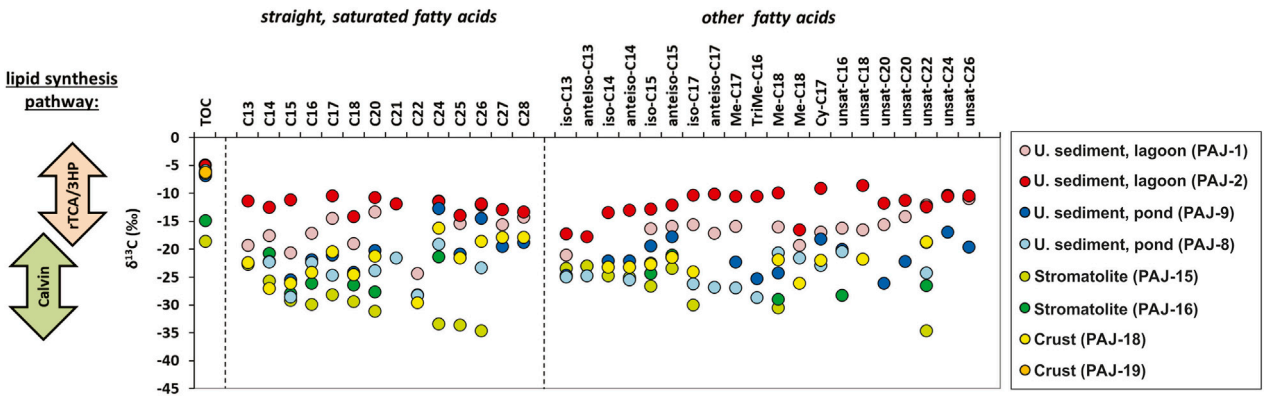

FIGURE 8
Compound-specific isotopic composition of carbon ($\delta^{13}C$) for the fatty acids identified in the SP samples, including two unconsolidated ("U.") sediments from the lagoon (PAJ-1 and PAJ-2); two stromatolites (PAJ-15 and PAJ-16); two unconsolidated sediments from ponds (PAJ-8 and PAJ-9), and crusts composed mainly of gypsum (PAJ-18) and halite (PAJ-19). The isotopic composition of total organic carbon (TOC) is shown together with that of straight-chain saturated fatty acids (C_n), and other configurations (*iso*, *anteiso*, trimethylated, cyclopropyl, and unsaturated). Colored arrows on the left indicate canonical biomass $\delta^{13}C$ values associated with the Calvin cycle (green arrow) and other carbon fixation pathways (orange arrow), which exhibit less fractionation against the heavier isotope $\delta^{13}C$ (i.e., rTCA, 3HP, 3HP/4HB and/or DC-4HB).

from −12 to −21‰), the 3HP bicycle ($\delta^{13}C$ from −4 to −15‰), the 3HP/4HB bicycle and/or the DC-4HB pathways ($\delta^{13}C$ from ca. −8 to −12‰; van der Meer et al., 2000; Hayes, 2001). The $\delta^{13}C$ composition of the fatty acids identified in unconsolidated sediments from the lagoon (PAJ-1 and PAJ-2) was consistent with rTCA pathway, while those in crust (PAJ-18), stromatolites (PAJ-15 and PAJ-16), and unconsolidated sediments from ponds (PAJ-8 and PAJ-9) corresponded more closely to the CBB cycle.

Overall, stromatolites (PAJ-15 and PAJ-16) and unconsolidated sediment from ponds near the terrace (PAJ-9) exhibited the most CBB-like isotopic signatures (i.e., the most ^{13}C-depleted or negative $\delta^{13}C$ values, −18.5 and −14.8‰). In contrast, two unconsolidated sediments from the lagoon (PAJ-1: −6.4‰, PAJ-2: −4.9‰) and from ponds (PAJ-8: −5.9‰) displayed less negative $\delta^{13}C$ values, suggesting compatibility with rTCA, 3HP, 3HP/4HB and/or DC-4HB pathways (Figure 8). The isotopic composition of the remaining samples (i.e., PAJ-9 and PAJ-18) reflected a possible combined contribution of different metabolic pathways, including the synthesis of low C chain fatty acids by photoautotrophic microorganisms, together with microbial degradation and re-synthesis of fatty acids with heavier isotopic ratios.

DNA abundance and sequencing data

Nucleic acid extraction yielded 9.1–242 ng·μL^{-1} (wet weight). DNA purity was acceptable across samples (mean A_{260}/A_{280} = 1.84; A_{260}/A_{230} = 1.72), except for PAJ-11, PAJ-12, and PAJ-13, which showed low DNA concentrations (Supplementary Table S10).

Illumina sequencing of the V1–V3 (bacterial) and V3–V4 (archaeal) 16S rRNA regions generated 155,211 and 606,367 raw reads from 18 to 16 samples, respectively. After DADA2 processing, 14 bacterial and 13 archaeal datasets remained, yielding 153,403 and 606,261 high-quality paired reads, corresponding to 1,519 bacterial and 763 archaeal ASVs. Read lengths ranged from 257 to 488 bp (bacteria) and 245–466 bp (archaea), consistent with the targeted hypervariable regions (Supplementary Table S11).

Overall community diversity and taxonomic composition

Across all samples from Flamencos Lagoon, microbial communities were dominated by six bacterial and two archaeal phyla, accounting for >98% of total reads (Figure 9; Table 2). Major bacterial phyla included Pseudomonadota (representing only Alphaproteobacteria and Gammaproteobacteria), Cyanobacteriota, Actinobacteriota, Chloroflexota, Planctomycetota, and Deinococcota (Figure 9A), while the main archaeal phyla included Halobacterota and Crenarchaeota (Figure 9B).

Pseudomonadota dominated stromatolites and crusts (~50%), mainly represented by Alphaproteobacteria (e.g., *Thalassospira* and other less-represented taxa), whereas the Gammaproteobacteria class was less represented in unconsolidated sediments and crusts. In stromatolites, the families Sphingomonadaceae (*Sphingomonas, Altererythrobacter*), Amorphaceae (*Acuticoccus*), and Caulobacteraceae predominated, while Rhodobacteraceae (*Roseovarius*), Rhizobiaceae, and Geminicoccaceae were more common in unconsolidated sediments and crusts (Figure 9C).

Cyanobacteriota were almost exclusively found in stromatolites, whereas chloroplast genes were detected predominantly in crusts and unconsolidated sediments (Figure 9C). Microscopy (Figure 6) and phylogenetic analyses (Supplementary Figure S10) revealed unicellular cyanobacterial morphotypes within the family Chroococcidiopsaceae (including *Aliterella* and *Gloeocapsa)*, as well as filamentous forms belonging to the orders Thermosynechococcales and Phormidesmiales (*Nodosilinea*) enclosed within gypsum crystals. In contrast, Actinobacteriota and Chloroflexota were more abundant in crusts and unconsolidated sediments, while Planctomycetota and Deinococcota occurred at

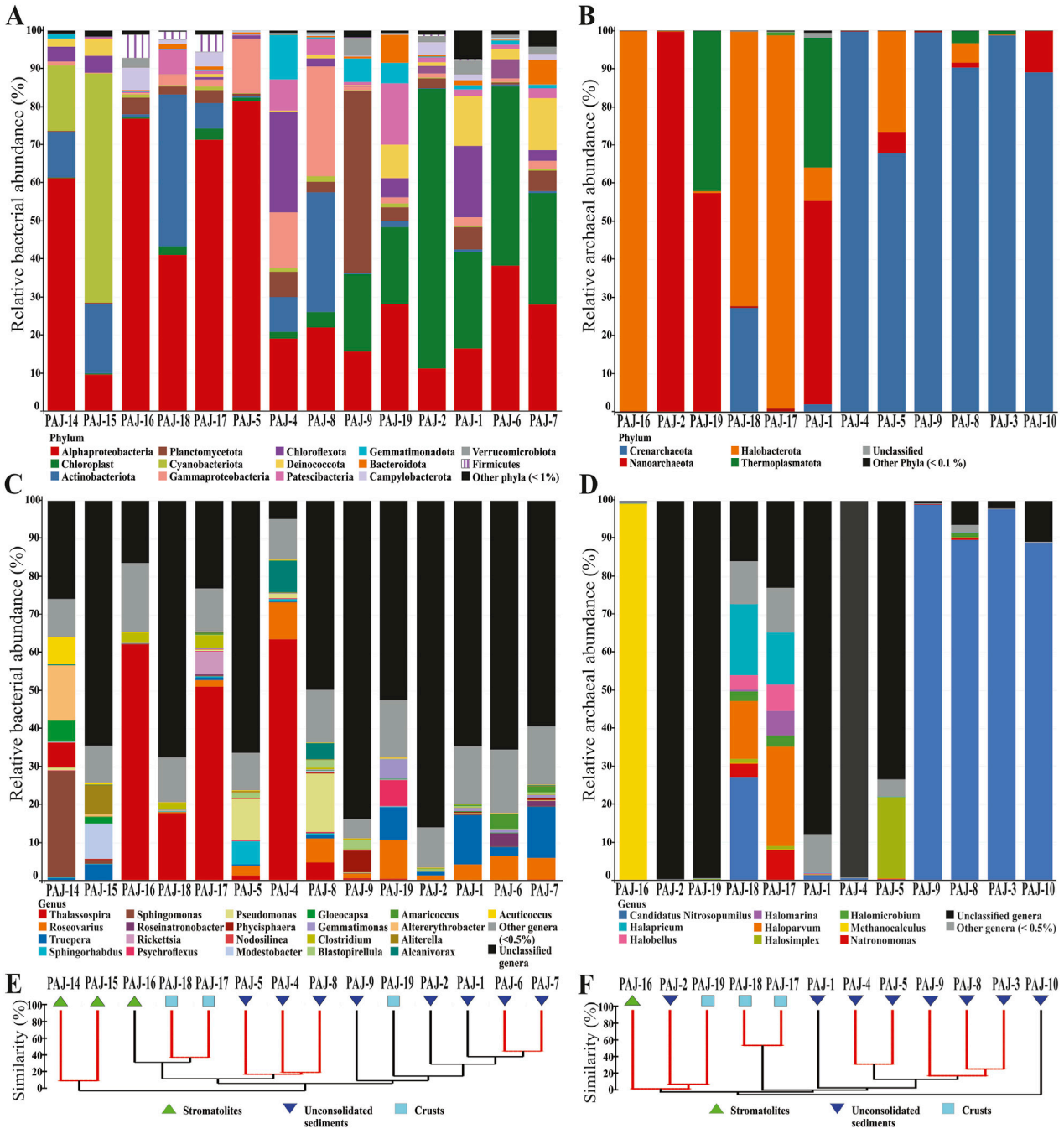

FIGURE 9
Bacterial (left) and archaeal (right) diversity in unconsolidated sediments, crusts, and stromatolites from the Salar de Pajonales. Community composition based on 16S rRNA gene sequencing is shown at: **(A,B)** phylum and **(C,D)** genus levels for Bacteria and Archaea. **(E,F)** SIMPROF cluster dendrograms based on Bray-Curtis similarity illustrate community structure across samples. Red lines indicate clusters with no significant differences. Note: Phyla and genera representing <1% or <0.5% relative abundance are grouped as "Other" (black bars). Note: High-quality, zoomable PDF versions of this figure are available.

lower relative abundances across all habitats. Minor phyla (<3%) were also detected across crusts and sediments.

In drier samples, archaeal communities were dominated by a single phylum, while unconsolidated sediments exhibited greater taxonomic diversity. Crenarchaeota, mainly *Candidatus Nitrosopumilus* (54% in sediments, 14% in crusts), and other Nitrosopumilaceae members prevailed in unconsolidated sediments, accompanied by Nanoarchaeota and Thermoplasmatota. In contrast, Halobacterota dominated stromatolites and crusts but represented only 6% of sediment communities. Within stromatolites, *Methanocalculus* accounted for nearly all Halobacterota reads, whereas crusts displayed higher

TABLE 2 Summary of biosignature-related features identified in this study, following the criteria proposed by Hays et al. (2017).

Biosignature-related features	Procedure/Relationship	Stromatolites		Crusts	Unconsolidated sediments	
		Bottom part	Upper part		Lagoon	Ponds
Macroscale to mesoscale observations by eye						
Morphology	Observations (Supplementary Figures S4–S6)	Centimeter-thick laminated layers with a hollow core	Radially oriented selenite crystals, 15 cm long	Cerebroid and globular morphologies	Brown and black unconsolidated sediments	
Color colonization signs	Observations (Supplementary Figures S4–S6)	No observed pigmentations	Green and pink pigmentations	Grey pigmentation	Green, and red biofilms interspersed with sediments	
Structural, textural, crystallographic, mineralogical, and microfossil characterization						
Micro structures/Textures	Petrographic observations (Figure 3)	Internal lamination and entombed diatom frustules	Micritized organic gels in the horizontal cleavage planes of the crystal	Not studied	Not studied	
	Elemental distribution using μXRF (Figure 4)	Micro-layering of both Ca-S- interspersed with Fe-Si-bearing minerals	Fishtail of both Ca-S- bearing and Si-Fe-bearing minerals	Not studied	Not studied	
Predominant minerals	DRX (Table 1)	Gypsum		Halite and gypsum	Gypsum, Na-Ca feldspars, and phyllosilicates	
Crystal appearance	FE-SEM-EDS (Figure 5)	Lenticular formations agglutinated with Mg-Si aggregates	Micrometric, subhedral gypsum crystals in varied orientations and rounded Mg-Si aggregates.	Not studied	Not studied	
Microfossil indicators	FE-SEM-EDS (Figure 5)	Gas bubble vestiges, abundant diatom frustules and micritized filamentous cells.	Alveolar calcite texture and less diatom frustules	Not studied	Not studied	

(Continued on the following page)

10.3389/fspas.2025.1693302

TABLE 2 (*Continued*) Summary of biosignature-related features identified in this study, following the criteria proposed by Hays et al. (2017).

Biosignature-related features	Procedure/Relationship	Stromatolites		Crusts	Unconsolidated sediments	
		Bottom part	Upper part		Lagoon	Ponds
Organic biosignatures						
Pigments	CLSM (Figure 6; Supplementary Figure S8; Supplementary Table S8)	No pigments observed	Presence of PC, APC, APC-B, and Chl a in unicellular cells and CAR, UDM, and PE in filamentous cells	Not studied	Not studied	
Abundant biosphere (<99% of total recovery) based on DNA	Alphaproteobacteria (photoheterotrophs; Figures 9A–C)	Thalassospiraceae (*Thalassospira*), Sphingomonadaceae (*Sphingomonas* and *Altererythrobacter*), Amorphaceae (*Acuticoccus*), and Caulobacteraceae families (10–77%)		Thalassospiraceae (*Thalassospira*), Rhodobacteraceae (*Roseovarious*, *Rhodobaca*, and *Limibaculum*), and Geminicoccaceae families (28–71%)	Thalassospiraceae (*Thalassospira*), Rhodobacteraceae (*Roseovarious*), Rhizobiaceae, and Geminicoccaceae families (11–81%)	
	Gammaproteobacteria (Hydrocarbon degraders, anoxygenic sulfur oxidizers; Figures 9A–C)	-		*Salinisphaera (2–3%)*	Families such as: Alcanivoraceae (*Alcanivorax*), Chromatiaceae (*Candidatus Thiobios*), pseudomonadaceae (*Pseudomonas*), Idiomarinaceae (2–28%)	
	Cyanobacteria (oxygenic phototrophs; Figures 9A–C)	Chroococcidiopsaceae (*Aliterella*, *Gloeocapsa*, *Dactylococcopsis*), and Nodosilineaceae (*Nodosilinea*) families (1–60%)		Chloroplast genes (3–20%)	Chloroplast genes (1–73%)	
	Actinobacteriota (desiccation-tolerant; Figures 9A–C)	Frankiales (Geodermatophilaceae), Micrococales (Intrasporangiaceae), and Euzebyales (Euzebyaceae) orders (1–18%)		Nitriliruptorales order (<1–7%)	Acidimicrobiia class (<1–31%)	
	Chloroflexota (anoxygenic phototrophs; Figures 9A–C)	Kallotenuales and Thermomicrobiales order (<1–4%)		Anaerolineae class (1–5%)	Anaerolineae class (1–26%)	
	Planctomycetota (heterotrophic biofilm formers; Figures 9A–C)	-		Phycisphaerae class (2–4%)	*Phycisphaerae and Planctomycetes (e.g., Blastopirellula) classes* (<1–48%)	
	Deinococcota (radiation-resistant; Figures 9A–C)	*Truepera (2–4%)*		*Truepera (<1%)*	*Truepera (<1–13%)*	
	Other bacterial phyla (Figures 9A–C)	Firmicutes		Patescibacteria, parcubacteria, Gemmatimonadota, bacteroidota, and Firmicutes	Parcubacteria, Gemmatimonadota, and bacteroidota	

(Continued on the following page)

10.3389/fspas.2025.1693302

TABLE 2 (*Continued*) Summary of biosignature-related features identified in this study, following the criteria proposed by Hays et al. (2017).

Biosignature-related features	Procedure/Relationship	Stromatolites		Crusts	Unconsolidated sediments	
		Bottom part	Upper part		Lagoon	Ponds
	Crenarchaeota (Ammonia oxidizers; Figures 9B–D)	-		Candidatus *Nitrosopumilus (<1–27%)*	Candidatus *Nitrosopumilus* and members of family Nitrosopumilaceae (<1–89%)	
	Halobacterota (Halotolerant; Figures 9B–D)	*Methanocalculus (~99%)*		*Haloparvum, Halopricum, Natronomonas, Halobellus, Halomarina, Halomicrobium, Halolamina,* and *Halobacterium (<1–97%)*	*Halosimplex (<1–20%)*	
	Other archaeal phyla (Figures 9B–D)	-		-	Nanoarchaeota (Woesearchaeales), Thermoplasmatota (*Thermoplasmata*)	
Lipid biomarkers related to	Cholesterol, stigmastanol, β-sitosterol, and brassicasterol ($\mu g \cdot g^{-1}$; eukaryotes; Figure 7A)	0–0.084		0.620–0.980	0–1.1	
	Iso and *anteiso* configuration ($\mu g \cdot g^{-1}$; bacteria; Figure 7B)	0.005–0.017		0.028–0.037	0.014–1.3	
	Crocetane and dihydrophytol ($\mu g \cdot g^{-1}$; archaea; Figure 7C)	0.097–0.690		0.91–0.92	0–1.2	
	Phytol ($\mu g \cdot g^{-1}$; photoautotrophs; Figure 7D)	0–0.050		0.170–0.800	0–0.36	
	7Me-C17, 8-heptadecene, 9-nonadecene, 16:1ω7, 18:1ω7, and18:1ω ($\mu g \cdot g^{-1}$; cyanobacteria; Figure 7E)	0.001–0.620		0.004–0.050	0.004–2.5	
	Brassicasterol ($\mu g \cdot g^{-1}$; Figure 7F; diatoms)	0–0.082		0–0.091	0–0.05	
	Potential metabolic pathway (Figure 8)	Dominance of Calvin cycle		Mix of Calvin cycle and rTCA, DC/4-HB, and/or 3-HP/4-HB pathways	Mix of Calvin cycle and rTCA, DC/4-HB, and/or 3-HP/4-HB pathways	
Molecule, elemental and isotopic composition						
Molecule	Moisture content (Table 1)	8–44% GWC		10–13% GWC	55–100% GWC	
		39–86% a_w		50–53% a_w	84–97% a_w	
Elements	TOC (%dw; Supplementary Table S9)	0.11–0.25		0.07–0.09	0.5–0.85	
	TN (%dw: Supplementary Table S9)	-		0.02	0.06–0.12	

(Continued on the following page)

10.3389/fspas.2025.1693302

10.3389/fspas.2025.1693302

TABLE 2 (*Continued*) Summary of biosignature-related features identified in this study, following the criteria proposed by Hays et al. (2017).

Biosignature-related features	Procedure/Relationship	Stromatolites		Crusts	Unconsolidated sediments	
		Bottom part	Upper part		Lagoon	Ponds
Isotopes	δ^{15}N-Total (‰; Supplementary Table S9)	7.7		7.6–11.3	11.1–15.7	
	δ^{13}C-OC (‰; Supplementary Table S9)	−18.51 to −14.78		-6.36 to −6.16	-6.84 to −4.89	
Result		Re-colonized		Colonized	Colonized	
Possible scenarios		Preservation		Habitability and preservation	Habitability	

genus-level diversity (Supplementary Figure S5A), including *Haloparvum*, *Halopricum*, *Natronomonas*, and other minor taxa. Cluster analysis showed distinct community groupings by sample type (Figures 9E,F).

Finally, a Venn diagram comparing bacterial and archaeal genera revealed 49 bacterial (Figure 9B) and 8 archaeal genera shared among all environments (Supplementary Figure S9C). Cyanobacteria and Halobacterota were enriched in stromatolites, whereas Nanoarchaeota prevailed in sediments (Supplementary Table S14).

Richness and diversity indices

Overall, the results presented in Supplementary Table S15 revealed distinct community patterns across sample types. Bacterial diversity and richness were highest in unconsolidated sediments, whereas archaeal diversity was more pronounced in crusts and stromatolites. The latter exhibited lower overall microbial diversity but greater dominance and community unevenness.

Microbial distribution with respect to environmental variables

Statistical analysis (p-value <0.05) identified key environmental variables influencing bacterial and archaeal α-diversity (Supplementary Table S16). Bacterial diversity increased with water availability but decreased with higher gypsum and epsomite concentrations, whereas archaeal diversity declined with increasing water content and was positively associated with sylvite, suggesting distinct adaptive strategies to moisture and salinity gradients.

Principal Coordinates Analysis (PCoA) revealed clear community structuring across samples. Bacterial assemblages formed four distinct clusters among unconsolidated sediments, crusts, and stromatolites (10%–20% similarity), each correlated with multiple variables (Figure 10A) and dominant phyla (Figure 10B). In unconsolidated sediments, Desulfobacteriota and Chloroplast-related sequences were associated with higher water content and silicate minerals (phyllosilicates, quartz, and Na-Ca feldspars), whereas Abditibacteriota and Cyanobacteriota in stromatolites correlated with gypsum, magnetite, and epsomite. Firmicutes, Alphaproteobacteria, and Campylobacterota were shared between crusts and unconsolidated sediments.

Similarly, archaeal communities clustered into three groups (5% similarity) corresponding to unconsolidated sediments and crusts (Figures 10C,D). Crenarchaeota in unconsolidated sediments were associated with higher water content and silicates, while Nanohaloarchaeota and Halobacterota in crusts correlated with sylvite and polyhalite, indicating the influence of mineral composition on community assembly.

Overall, bacterial diversity was shaped by water availability, substrate type, and site, whereas archaeal diversity reflected site-specific and mineralogical controls, highlighting the strong environmental selection imposed by substrate and moisture gradients.

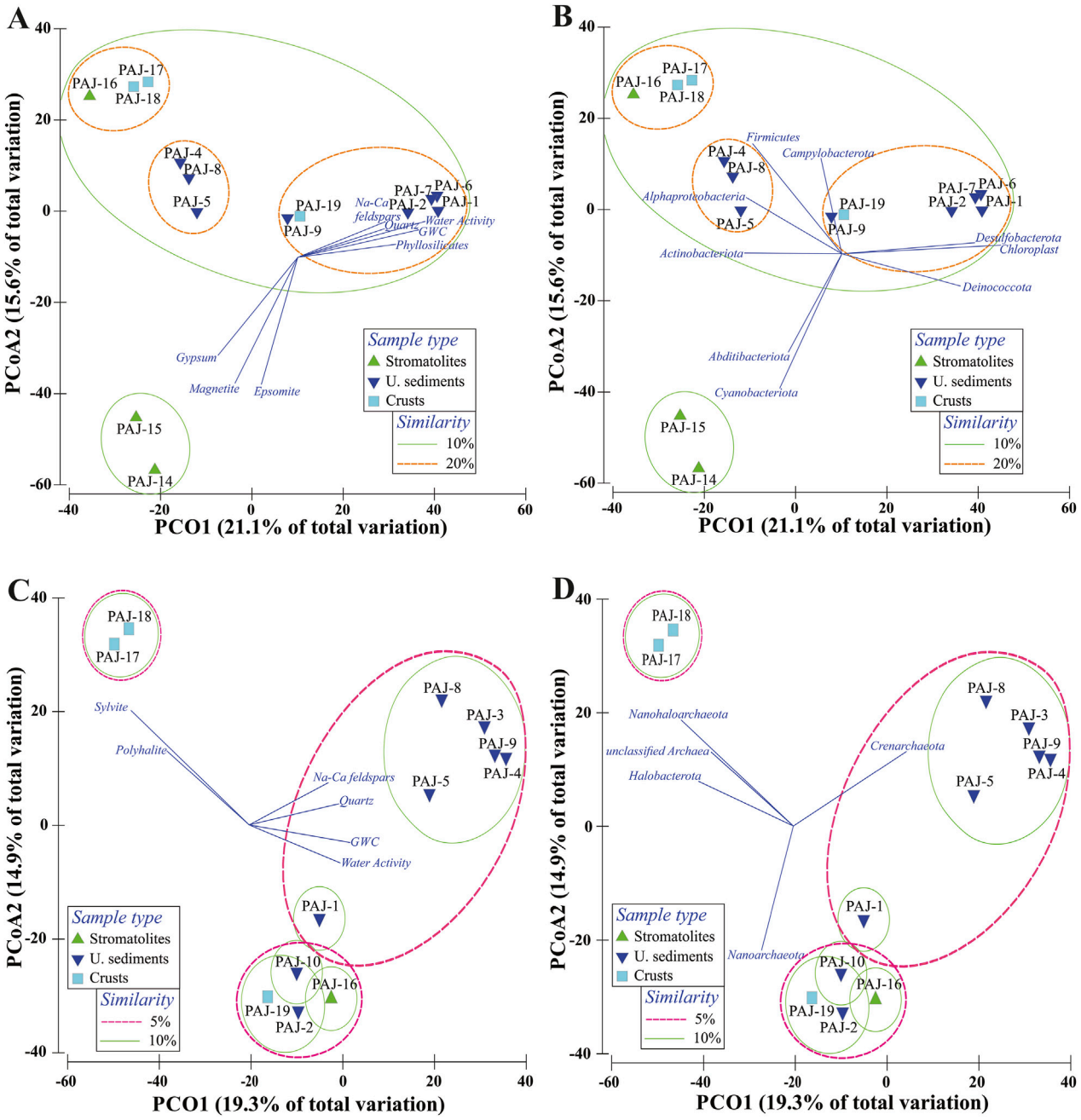

FIGURE 10
Principal coordinates analysis (PCoA) of Bray-Curtis similarities based on bacterial **(A, B)** and archaeal **(C, D)** 16S rRNA sequences from unconsolidated sediment, crust, and stromatolite samples. The analysis includes Pearson correlation vectors (r >0.5) representing GWC, a_w, and mineralogical compositions **(A, C)**, as well as phylum- and class-level distributions **(B, D)**. The pink, green, and orange cluster lines indicate sample groupings based on 5%, 10%, and 20% similarity in microbial composition, respectively.

Discussion

Geological and climatic context and relic gypsum stromatolites

The Salar de Pajonales presents challenges in the search for extinct and extant biosignatures within gypsum fossil structures exposed on the terraces (PAJ-13 to PAJ-16; Figure 1C; Supplementary Figure S5). Although the age of these gypsum features was not determined in this study, research on similar structures in the Salar de Gorbea (~30 km northwest of Pajonales, which shares a similar geological setting) suggested they formed between 6,400 and 4,000 years before present (Pueyo et al., 2021).

Observations revealed that the terrace of Flamencos Lagoon contains well-preserved gypsum stromatolites with repetitive lamination defined by alternating gypsum and thin microbial

laminae that include diatom frustules, authigenic carbonates, Mg-silicates, and trapped silicate grains (Figures 3–5). The multilaminated stromatolites exhibited folded and domal morphologies at the base, while the upper gypsum laminae tended to be planar and thicker. At the top, the stromatolites host extant endolithic microbial communities within pink and green layers. These pigmented layers (Supplementary Figures S5C,G) are indicative of biofilm fabrics (Rodríguez, 2018; Ercilla, 2019) and have also been described in gypsum domes in northern sections of the Salar de Pajonales (Warren-Rhodes et al., 2023).

The preservation of abundant microbial communities was particularly notable given the extreme climatic conditions of SP, characterized by prolonged aridity (13–36% RH), intense solar radiation (800–1,317 $W{\cdot}m^{-2}$; Figure 2E), and strong winds (up to 31 $m{\cdot}s^{-1}$; Supplementary Figure S2A), all of which further exacerbate surface desiccation (Supplementary Table S17). This stressful context, in which endolithic communities persist, can be defined not only by moisture constraints but also by oxidative and nutrient-limiting stress. Moreover, sulfate-rich habitats with low nutrient availability are known to exhibit strong oxidant activity that limits microbial abundance (Valdivia-Silva et al., 2016), reinforcing that life in these settings must adapt to moisture and oxidative constraints.

The SP remains underrepresented in regional climate studies (Supplementary Table S17), which have largely focused on lower-altitude sites of the Atacama Desert characterized by hyperaridity and exceptionally low precipitation (McKay et al., 2003; de Los Rios et al., 2010; Finstad et al., 2016; Azua-Bustos et al., 2018; Pfeiffer et al., 2021). Although SP experiences comparably arid conditions, the data revealed significant moisture anomalies, with prolonged dry periods and short-lived wet events (June 6–10, 2017, and 8 September 2019) marked by elevated air relative humidity and soil moisture. These transient episodes may have delivered critical pulses of water to gypsum-rich habitats such as stromatolites and crusts. The temporal alignment of these pulses with regional precipitation records suggests that moisture incursions—possibly as snow or freezing rain—also reached SP, potentially triggering microbial reactivation.

Fossil biosignatures in lower stromatolite layers

In the lower part of the stromatolites, we identified multiple features consistent with well-established biosignatures (Table 2; Hays et al., 2017), including laminated fabrics with alternating layers of calcium sulfate, silicates, and iron oxides (Figure 4). These layers contained hallmarks of past microbial activity, such as numerous preserved diatom frustules and micritized filamentous cell structures. The presence of gas bubble vestiges may also represent a biosignature; alternatively, they could result from volcanic processes. Micro-laminated textures with enhanced porosity resembled carbonate-coated grains commonly attributed to microbial mediation (Boelts et al., 2021), suggesting biologically influenced mineralization.

Mineral precipitates, such as gypsum spherulites (Figure 3C) and granular Mg–Si aggregates (Figure 5D), were embedded within laminae and associated with degraded diatom frustules, cell sheaths, and mineralized organic remnants in the lower stromatolite layers. These associations were consistent with microbial involvement in gypsum precipitation (Thompson and Ferris, 1990) and Mg-clay formation (del Buey et al., 2021; Oehlert et al., 2022).

Previous studies have demonstrated that organic matter can play a fundamental role in controlling gypsum morphology and growth. Both experimental and natural examples demonstrate that extracellular polymers and organic films can act as nucleation templates, promoting the formation of fibrous, lenticular, and spherulitic gypsum crystals under variable degrees of supersaturation (Cody and Cody, 1988; Vogel et al., 2010). Likewise, Cabestrero and Sanz-Montero (2016) and Cabestrero et al. (2022) reported that microbial mats and organic substrates can locally modify brine chemistry, influencing gypsum habit, lamination, and crystal orientation through microbial exudates and microenvironmental pH shifts.

The occurrence of such mineral-microbe interaction records in these lower sections, combined with textural evidence of dissolution and recrystallization patterns, suggests the presence of liquid water within the rock for an extended period. In contrast, the upper millimetric layers of the stromatolites lacked diatom remains and hosted extant microbial communities characterized by pigmented layers and active cyanobacterial cells (Figure 6A). This contrast suggests a temporal shift in community composition, where diatom remnants in deeper layers represent fossilized biosignatures from earlier hydrological periods, while current microbial life is dominated by photosynthetic cells adapted to the present arid conditions.

The contrasting preservation of diatoms is consistent with mineralogical and textural evidence, where dissolution and reprecipitation of silica phases in deeper layers point to geochemical controls, whereas the upper layers, dominated by gypsum and halite, indicate more saline conditions that are less favorable for diatom development.

Chloroplast genes detected in unconsolidated sediments composed of detrital minerals from volcanic rocks (e.g., Na–Ca feldspars) were predominant and phylogenetically related to uncultured diatom chloroplasts (Supplementary Figure S10). Similar but less abundant sequences were also found in gypsum stromatolites and crusts at SP. The few diatom frustules observed in stromatolites resembled members of the Bacillariophyceae family and differed from those reported in other gypsum endolithic habitats described in Supplementary Table S1. These frustules likely represent new taxa within *Amphora* and *Surirella Sella* (Díaz and Maidana, 2005). As key fossil biosignatures, they record a transition from lacustrine to evaporitic regimes at SP, providing insights into paleoenvironmental conditions.

Extant endolithic communities and upper layer microhabitats

In the upper part of the stromatolites, just millimeters beneath the surface, extant microbial communities composed of pigmented biolayers and active cyanobacteria dominated throughout the 4-year sampling campaign, while diatoms were absent. This pattern suggests a temporal shift in community composition: fossilized diatom signatures reflect past lacustrine conditions, whereas the

present microbial communities indicate adaptation to the current arid environment, taking advantage of gypsum as a habitable mineral substrate.

Microscopically, endolithic microorganisms were associated with calcite aligned along vertical gypsum crystal planes, including exfoliation surfaces and twin planes (Figure 3G–I). These microbial processes progressively brecciated the large gypsum crystals, creating micro-niches around the fragmented crystals. Such niches provided protected microenvironments that supported microbial colonization, as evidenced by the presence of both active and inactive cells embedded within fissures. The persistence of these communities under extreme environmental conditions underscores the astrobiological significance of these structures as indicators of habitability.

Microbial community dynamics in gypsum and associated sedimentary environments

Bacterial and archaeal communities in SP were primarily structured by sample type, moisture availability, and mineralogy, particularly gypsum *versus* Na–Ca feldspars and phyllosilicates (Figure 10). Low-moisture gypsum samples harbored reduced diversity, whereas more hydrated unconsolidated sediments supported richer microbial assemblages.

Across the site, 49 bacterial and 8 archaeal taxa were shared among samples, indicating a functionally specialized ecosystem adapted to extreme conditions. Dominant phototrophs such as Chroococcidiopsaceae underscored the importance of photosynthetic primary production in nutrient-poor settings (Wierzchos et al., 2015). The coexistence of both aerobic (e.g., Thalassospira; Tsubouchi et al., 2014) and anaerobic heterotrophs (e.g., Woesearchaeales; Liu et al., 2018) suggested a dynamic interplay between metabolisms, likely influenced by diel oxygen fluctuations. In addition to these nutrient cycling microorganisms, both radiation- and desiccation-resistant taxa occurred in all SP samples. Chemoorganotrophs resistant to ionizing radiation (e.g., Truepera; Albuquerque et al., 2005) and mixotrophic Arcobacteraceae (Li et al., 2024) point to adaptations to UV radiation and variable organic carbon availability.

Gypsum stromatolites were dominated by aerobic heterotrophic Actinobacteria and Alphaproteobacteria (e.g., *Sphingomonas*, *Altererythrobacter*, and *Acuticoccus*) known for their salt tolerance and carotenoid production in saline environments (Azpiazu-Muniozguren et al., 2021; Fuentes et al., 2021; Li et al., 2021). Actinomycetes and nitrogen-fixing Frankiales, previously reported in hyperarid Atacama environments (Demergasso et al., 2023; Bartholomaus et al., 2024), exhibit resistance to desiccation, UV radiation, and osmotic and temperature extremes (Oshone et al., 2017). Moreover, *Modestobacter caceresii* carries stress-response genes associated with oxidative, osmotic, thermal, UV, and salinity stress, enabling survival under the extreme hyperarid conditions of the Atacama Desert (Busarakam et al., 2016). The presence of *Methanocalculus*, an alkaliphilic and lithoheterotrophic methanogen, further highlights potential methane cycling in this environment (Sorokin et al., 2015).

Microbial taxa in unconsolidated sediment and crust communities also reflected adaptations to salinity. Taxa such as *Roseovarius*, *Pseudomonas*, *Gemmatimonas*, and members of the phylum Crenarchaeota (e.g., Nitriliruptoraceae and *Candidatus Nitrosopumilus*) have been previously reported in lakes and wetlands of the Salar de Atacama (Fernandez et al., 2016; Núñez Salazar et al., 2020; Ramos-Tapia et al., 2022). These archaeal taxa synthesize compatible solutes (e.g., ectoine and hydroxyectoine) that protect cells from osmotic pressure and desiccation while contributing to autotrophy and potassium homeostasis (Vargas et al., 2006; Walker et al., 2010). Similarly, *Salinibacter* and *Psychroflexus*, detected in crusts and unconsolidated sediments, are halophilic bacteria that degrade complex polysaccharides and contribute to carbon cycling in hypersaline, oligotrophic environments (Demergasso et al., 2004; Demergasso et al., 2008; Vignale et al., 2021). Their presence reinforces that microbial resilience in SP depends not only on moisture retention but also on nutrient recycling.

Specific aerobic organoheterotrophic groups such as Anaerolineaceae and Phycisphaeraceae, found exclusively in SP unconsolidated sediments, were previously identified in microbial mats and rhizome-associated concretions in Laguna Tebenquiche, Atacama Desert (Fernandez et al., 2016). Halobacterota genera such as *Haloparvum* and *Natronomonas* dominated in crusts, similar to communities from endoevaporites of Laguna Barros Negros (Demergasso et al., 2004; Vignale et al., 2021). Other lesser-known Alphaproteobacteria detected only in crusts at SP included *Rhodobaca,* found in Siberian lakes (Boldareva et al., 2008), and *Limibaculum*, described from Korean muds (Shin and Brangwynne, 2017), highlighting broader ecological connections with other hypersaline and sedimentary environments.

Overall, gypsum and halite habitats hosted both UV- and desiccation-resistant taxa, whereas unconsolidated sediment communities were more closely linked to aquatic environments. These findings support the interpretation that gypsum, like sepiolite, can store and supply moisture, playing a vital role in sustaining microbial life in arid settings. However, the mechanisms differ: gypsum incorporates water as an essential component of its crystal structure, whereas sepiolite retains it within channels and pores through a wider range of bonding states. Although not directly comparable in their bonding environments, both minerals provide essential water–mineral interactions that are critical to their physical properties and potential as microbial habitats (Wierzchos et al., 2015; Huang et al., 2020).

Altogether, microbial communities inhabiting gypsum stromatolites and halite crusts exhibit traits linked to osmotic stress, UV resistance, and nutrient scarcity, while unconsolidated sediment communities show closer ties to plant-associated aquatic environments (Ramos-Tapia et al., 2022). These findings suggest that gypsum can retain and supply moisture, playing a critical role in shaping microbial life under extreme desert conditions.

The gypsum samples analyzed here were collected in October—outside the wet season—thus representing minimum water availability conditions. Despite intense solar radiation and strong winds that enhance desiccation, gypsum stromatolites retained 10%–13% GWC and 0.50–0.53 a_w, values approaching the physiological lower limit for microbial metabolism (0.585 a_w; Huang et al., 2020). Similar intrinsic moisture conditions were measured in Antarctic gypsum crusts containing endolithic communities, which maintained ~4.7% GWC under

subzero temperatures (Hughes and Lawley, 2003). Comparable environmental conditions have also been documented for gypsum outcrops across the Atacama Desert, where relative humidity ranges between 15.2% and 47.9% (Supplementary Table S1; Wierzchos et al., 2015), between 39.7% and 58.8% in the arid environment of Fayum, Egypt (Taher, 2014), and around 80% in Alexander Island, Antarctica (Hughes and Lawley, 2003). Together, these observations indicate that both internal (GWC, a_w) and external (RH) moisture conditions enable gypsum to sustain microbial life across extreme climates, from cold polar deserts to hyperarid high-altitude settings.

Cyanobacterial morphotypes and photosynthetic pigments as indicators of cell viability

Microscopic and phylogenetic analyses of the upper stromatolite layers revealed a strong correlation between gypsum and the phylum Cyanobacteria. Unicellular coccoid (morphotype 1) and filamentous cyanobacteria cells (morphotypes 2 and 3) appeared to play a role in the dissolution of large gypsum crystals and the formation of lenticular gypsum, as observed in previous studies (Cody and Cody, 1988; Vogel et al., 2010).

Morphotype 1 (0.3%–47%) was most similar to members of Chroococcidiopsaceae from quartz hypoliths in China (Pointing et al., 2007) and, to a lesser extent, to *Gloeocapsa* sp. isolated from a moderately hot spring in El Tatio, Chile (Mukaiyama et al., 2019); morphotype 3 matched *Nodosilinea nodulosa* isolated from rock surfaces at the shoreline of Montauk Point, New York, United States (Perkerson et al., 2011), whereas morphotype 2 resembled the families Coleofasciculaceae, Phormidiaceae, and Thermosynechococcaceae (Supplementary Figure S10; Supplementary Table S12).

Confocal microscopy revealed *chlorophyll a* and carotenoids in active coccoid and inactive filamentous cells, respectively (Figure 6). Active cells within gypsum crystals can retain thylakoid structures and produce the UV-protective pigment scytonemin, similar to endoliths in halite pinnacles from Yungay and Salar Grande (Roldán et al., 2014; Wierzchos et al., 2015). Carotenoid-rich cyanobacteria may contribute to both UV protection and photosynthesis (Nemeckova et al., 2023). In contrast, chlorosis and pigment loss in inactive cells, likely resulting from increased membrane permeability and pigment degradation, highlight the dual role of gypsum as both a microbial refuge and a medium for biosignature preservation.

Lipid and isotopic biomarkers and functional adaptations

To further distinguish between ancient and modern microbial communities, we examined lipid biomarkers across different samples (Figure 8). In gypsum stromatolites and crusts, lipid compounds likely represent a mixture of signals from both extant and fossilized microorganisms, owing to their stratified structure and encapsulation potential. In contrast, lipids detected in unconsolidated sediments reflected higher water availability and microbial activity, likely derived from living microbial populations.

The presence of lipid biomarkers associated with cyanobacteria, photoautotrophs, and archaea, together with the detection of eukaryotic sterols such as brassicasterol, cholesterol, stigmastanol, and β-sitosterol, indicates a mixed but prokaryote-dominated microbial community (Bergamino et al., 2016). The predominance of prokaryotic biomarkers supports the interpretation that primary productivity was mainly sustained by cyanobacteria and archaea, while the eukaryotic contribution likely derived from minor inputs of diatoms, algae, or detrital organic matter. This interpretation is further supported by $\delta^{13}C$ compositions and 16S rRNA gene sequencing, which corroborate the presence of cyanobacteria and archaea (e.g., Nanoarchaeota) within gypsum crystals in stromatolites.

Additional evidence comes from the detection of lipid biomarkers in gypsarenite crusts from seawater evaporation ponds in Mexico, specifically monomethylalkanes (MMAs) and 7-methylheptadecane, associated with *Euhalothece* and *Leptolyngbya*, respectively (Jahnke et al., 2014). These findings suggest that fissures and cracks within gypsum may serve as refuges for surviving unicellular and filamentous prokaryotic colonizers.

Lipid and isotopic data also suggest the dominance of autotrophic pathways related to the synthesis of cell-membrane compounds (Hugler and Sievert, 2011). These include the CBB cycle, common among oxygenic phototrophs (e.g., cyanobacteria and algae), and the contribution of other pathways used by anoxygenic photoautotrophs, such as purple sulfur bacteria (Gammaproteobacteria, detected in both crust and unconsolidated sediment samples; i.e., rTCA) and non-sulfur bacteria (members of Chloroflexota, present in all samples; i.e., 3HP bicycle).

To better understand autotrophic strategies in SP's modern microbial communities, we analyzed key carbon fixation pathways and their associated taxa. The rTCA cycle, used by green sulfur bacteria, including *Nitrospirae*, thermophilic Aquificales, and Deltaproteobacteria (Campbell and Cary, 2004; Bayer et al., 2021), was linked to Desulfobacteriota, specifically members of the Desulfocapsaceae and Desulfobacteraceae families, found only in unconsolidated sediments, albeit in low abundance (<1%). More notably, *Methanocalculus*, a lithoheterotrophic, alkaliphilic, salt-tolerant, and methanogenic archaeon (Sorokin et al., 2015), was dominant in stromatolite samples, suggesting a potential role in the rTCA cycle.

Additionally, members of Chloroflexaceae in stromatolites and unconsolidated sediments appear to utilize the 3HP bicycle (Hayes, 2001). Crenarchaeota detected in PAJ-9 and PAJ-8 unconsolidated sediments may engage in either the 3HP/4HB or DC/4HB cycles (Berg et al., 2010), highlighting functional metabolic diversity within these communities.

Habitability and biosignature preservation in gypsum

The ability of gypsum to simultaneously support microbial colonization and preserve biosignatures reinforces its value as a prime target in planetary exploration. Our findings from Salar de Pajonales align with those from other Mars-analog environments

(Hays et al., 2017; Jehlička et al., 2024), showing that gypsum minerals provide both protective microhabitats for extant life and a medium for fossil biosignature preservation. Gypsum's low thermal conductivity, light translucency, and hydrophilic properties may foster microbial survival during arid periods, while rapid sulfate precipitation promotes the entombment of organic matter and microbial remains (Schopf et al., 2012; Benison, 2019). Evaporitic systems worldwide demonstrate that sulfate minerals can trap and preserve biological materials within intercrystalline and intracrystalline spaces, shielding them from oxidation and degradation (Perl et al., 2021).

However, preservation efficiency is not constant. As shown by Pellegrino et al. (2024), alternating arid and humid phases can produce contrasting preservation states within a single gypsum crystal, wherein arid intervals enhance biosignature retention, whereas humid or anoxic episodes promote early diagenetic alteration and organic decay. This pattern aligns with the seasonal wet–dry cycles observed at SP (Figure 2), where episodic moisture fluctuations likely regulate microbial activity and biosignature preservation within gypsum layers.

Gypsum can record both living and ancient microbial communities, as illustrated by the stratified biosignatures at SP—from active, pigment-bearing cyanobacteria in surface layers to fossilized diatoms in deeper laminae. On Mars, widespread sulfate deposits and pseudomorphs after gypsum indicate past evaporitic environments (Kah et al., 2018). Studies in Gale and Jezero craters show that Ca-sulfate minerals formed through multiple episodes of precipitation and diagenesis (Vaniman et al., 2018; Rampe et al., 2020; Siljeström et al., 2024), with distinct generations documenting different aqueous conditions and preservation potentials (Jones et al., 2025).

Observations from SHERLOC (Scanning Habitable Environments with Raman and Luminescence for Organics and Chemicals), an instrument aboard the Perseverance rover of NASA's Mars 2020 mission, reveal variable hydration states in Jezero Crater sulfates consistent with aqueous alteration, highlighting the potential of such minerals to preserve biosignatures under suitable conditions (Phua et al., 2024).

In this context, the gypsum deposits at Salar de Pajonales provide an Earth analog for understanding the formation and preservation of Martian sulfate systems. Seasonal hydration–dehydration cycles at SP may parallel the diurnal water exchange processes proposed for Martian salts (Zorzano et al., 2024), while gypsum's attenuation of ultraviolet radiation (Carrier et al., 2019) could similarly protect organic matter. Together, these analogs underscore the role of sulfate minerals as transient habitats and long-term archives of biological activity, offering a framework to assess how mineralogy, water availability, and radiation interact to shape biosignature preservation on Mars.

Conclusion

In environments relevant to astrobiology, there is an inherent trade-off between habitability and biosignature preservation. The Salar de Pajonales (SP) exemplifies this balance, where climatic conditions favor the biosignature preservation within gypsum structures, while also supporting diverse and active microbial niches. Preservation may be enhanced by rapid burial and gypsum precipitation, which encapsulate biological materials in high-salinity environments.

Stromatolites at SP exhibit strong biosignature preservation supported by their layered morphology, mineral composition, and internal microtextures—including micritization, diatom frustules, and preserved microbial fabrics. The presence of phototrophs, including active Chroococcidiopsaceae and Nodosilineaceae within green and pink subsurface layers, further confirms ongoing microbial colonization and metabolic activity.

Although stromatolites provide excellent preservation potential due to their mineralogy and internal structures, unconsolidated sediments from Flamencos Lagoon and evaporitic ponds display greater microbial diversity and habitability but are more susceptible to environmental degradation. Shifts in microbial diversity across substrates, coupled with lipid and isotopic biomarkers, indicate that both active and fossil biosignatures co-occur, reflecting environmental changes over time.

These findings reinforce the astrobiological significance of gypsum as both a recorder of past life and a refuge for extant microbial activity. Ancient Martian environments with similar evaporitic deposits may have offered comparable conditions, making stromatolite-like structures compelling targets for life detection in future planetary missions. However, our results also emphasize that crusts and unconsolidated sediments represent valuable terrestrial analogs for biosignature exploration, as they exhibit greater microbial diversity than stromatolites. This suggests that diverse organic signals, though likely present at lower concentrations, could also be found in non-stromatolitic rocks on Mars.

Understanding how habitability and biosignature preservation intersect is therefore essential for guiding astrobiological exploration strategies beyond Earth.

Data availability statement

The datasets presented in this study can be found in online repositories. The names of the repository/repositories and accession number(s) can be found in the article/Supplementary Material.

Author contributions

CT-C: Conceptualization, Investigation, Supervision, Methodology, Project administration, Funding acquisition, Resources, Writing – review and editing, Formal Analysis, Software, Visualization, Validation, Writing – original draft, Data curation. CD: Funding acquisition, Writing – review and editing, Conceptualization, Resources, Supervision. ÓC: Methodology, Visualization, Validation, Writing – review and editing. GC: Conceptualization, Validation, Writing – review and editing. DC: Visualization, Conceptualization, Investigation, Data curation, Writing – review and editing, Resources. LS-G: Writing – review and editing, Conceptualization, Investigation, Resources, Data curation, Validation. VP: Investigation, Conceptualization, Funding acquisition, Writing – review and editing, Resources. KW-R: Validation, Writing – review and editing, Conceptualization. NC: Writing – review and editing, Conceptualization, Funding

acquisition, Resources. AE-V: Writing – review and editing, Data curation, Validation, Supervision. EC: Data curation, Writing – review and editing, Supervision. AM: Validation, Writing – review and editing. MES-M: Validation, Visualization, Conceptualization, Writing – review and editing.

Funding

The author(s) declared that financial support was received for this work and/or its publication. CT-C gratefully acknowledges support from the ANID National Doctoral Scholarship (No. 21181422). This research was also funded by the Broken Hill Proprietary (BHP) Minerals Americas Project 32002137 (2016–2020) under the direction of CD. Sample collection and *in situ* observations were funded by the NASA Astrobiology Institute (NAI) through grant NNA15BB01A, awarded to NC, Director of the Carl Sagan Center (SETI). LS-G, DC, and VP were supported by MCIN/AEI/10.13039/501100011033 and ESF+*Investing in Your Future* through grants RYC2018-023943-I (LS-G) and projects ESP2017-87690-C3-3-R (DC) and PID 2021-126746NB-I00 (VP and LS-G). Additional support was provided to MES-M, ÓC, and CT-C by MCIN/AEI/10.13039/501100011033 under project PID2021-123735OB-C22/C21.

Acknowledgements

The authors gratefully acknowledge the use of the CBAR laboratory facilities, Universidad Católica del Norte (UCN), Antofagasta, Chile, as well as the MAINI-UCN Scientific Equipment Unit for providing access to the FE-SEM SU5000 equipment with EDS and XRD D8 ADVANCE FIC Regional EQU-25 CONICYT instruments. We also thank Marian Barajas for supervising the preparation of thin sections at the Universidad Complutense de Madrid.

Conflict of interest

The author(s) declared that this work was conducted in the absence of any commercial or financial relationships that could be construed as a potential conflict of interest.

Generative AI statement

The author(s) declared that generative AI was not used in the creation of this manuscript.

Any alternative text (alt text) provided alongside figures in this article has been generated by Frontiers with the support of artificial intelligence and reasonable efforts have been made to ensure accuracy, including review by the authors wherever possible. If you identify any issues, please contact us.

Publisher's note

Supplementary material

The Supplementary Material for this article can be found online at: https://www.frontiersin.org/articles/10.3389/fspas.2025.1693302/full#supplementary-material

References

Abrajano, T. A., Murphy, D. E., Fang, J., Comet, P., and Brooks, J. M. (1994). Ratios in individual fatty acids of marine mytilids with and without bacterial symbionts. *Org. Geochem.* 21 (6-7), 611–617. doi:10.1016/0146-6380(94)90007-8

Albuquerque, L., Simoes, C., Nobre, M. F., Pino, N. M., Battista, J. R., Silva, M. T., et al. (2005). *Truepera radiovictrix* gen. nov., sp. nov., a new radiation resistant species and the proposal of Trueperaceae fam. nov. *FEMS Microbiol. Lett.* 247 (2), 161–169. doi:10.1016/j.femsle.2005.05.002

Allwood, A. C., Burch, I. W., Rouchy, J. M., and Coleman, M. (2013). Morphological biosignatures in gypsum: diverse formation processes of Messinian (approximately 6.0 Ma) gypsum stromatolites. *Astrobiology* 13 (9), 870–886. doi:10.1089/ast.2013.1021

Anderson, M. J., Gorley, R. N., and Clarke, K. (2008). *PERMANOVA+ for primer: guide to software and statistical methods*. First edition ed. Plymouth, United Kingdom: Primer-E Limited.

Awramik, S. M., Margulis, L., and Barghoorn, E. S. (1976). "Chapter 4.4 evolutionary processes in the formation of stromatolites," in. *Stromatolites*. Editor M. R. Walter (Amsterdam, The Netherlands: Elsevier), 20, 149–162. doi:10.1016/s0070-4571(08)71135-x

Azpiazu-Muniozguren, M., Perez, A., Rementeria, A., Martinez-Malaxetxebarria, I., Alonso, R., Laorden, L., et al. (2021). Fungal diversity and composition of the Continental solar saltern in Anana Salt Valley (Spain). *J. Fungi* 7 (12), 1074. doi:10.3390/jof7121074

Azua-Bustos, A., Fairen, A. G., Gonzalez-Silva, C., Ascaso, C., Carrizo, D., Fernandez-Martinez, M. A., et al. (2018). Unprecedented rains decimate surface microbial communities in the hyperarid core of the Atacama Desert. *Sci. Rep.* 8 (1), 16706. doi:10.1038/s41598-018-35051-w

Bartholomaus, A., Genderjahn, S., Mangelsdorf, K., Schneider, B., Zamorano, P., Kounaves, S. P., et al. (2024). Inside the atacama desert: uncovering the living microbiome of an extreme environment. *Appl. Environ. Microbiol.* 90 (12), e0144324. doi:10.1128/aem.01443-24

Bayer, B., Saito, M. A., McIlvin, M. R., Lucker, S., Moran, D. M., Lankiewicz, T. S., et al. (2021). Metabolic versatility of the nitrite-oxidizing bacterium *Nitrospira marina* and its proteomic response to oxygen-limited conditions. *ISME J.* 15 (4), 1025–1039. doi:10.1038/s41396-020-00828-3

Benison, K. C. (2019). The physical and chemical sedimentology of two high-altitude acid salars in Chile: sedimentary processes in an extreme environment. *J. Sediment. Res.* 89 (2), 147–167. doi:10.2110/jsr.2019.9

Benison, K. C., and Karmanocky, F. J. (2014). Could microorganisms be preserved in Mars gypsum? Insights from terrestrial examples. *Geology* 42 (7), 615–618. doi:10.1130/g35542.1

Berg, I. A., Kockelkorn, D., Ramos-Vera, W. H., Say, R. F., Zarzycki, J., Hugler, M., et al. (2010). Autotrophic carbon fixation in archaea. *Nat. Rev. Microbiol.* 8 (6), 447–460. doi:10.1038/nrmicro2365

Bergamino, L., Martínez, A., Han, E., Lercari, D., and Defeo, O. (2016). Trophic niche shifts driven by phytoplankton in sandy beach ecosystems. *Estuar. Coast. Shelf Sci.* 180, 33–40. doi:10.1016/j.ecss.2016.06.023

Bey, B. S., Fichot, E. B., and Norman, R. S. (2011). Extraction of high molecular weight DNA from microbial mats. *BioTechniques* 49 (53), e2887. doi:10.3791/2887

Bibring, J. P., Langevin, Y., Gendrin, A., Gondet, B., Poulet, F., Berthe, M., et al. (2005). Mars surface diversity as revealed by the OMEGA/Mars express observations. *Science* 307 (5715), 1576–1581. doi:10.1126/science.1108806

Bilskie, J. (2001). *Soil water status: content and potential*. Campbell Scientific, Inc. Available online at: https://s.campbellsci.com/documents/us/technical-papers/soilh20c.pdf (Accessed October 7, 2009).

Blazka, P., and Fischer, Z. (2014). Moisture, water holding, drying and wetting in forest soils. *Open J. Soil Sci.* 4, 174–184. doi:10.4236/ojss.2014.45021

Boelts, H. P., Ibarra, Y., and Hayzelden, C. (2021). The influence of benthic diatoms on the textures of carbonate-coated grains from a fluvial tufa spring in northern California. *J. Sediment. Res.* 90 (11), 1601–1613. doi:10.2110/jsr.2020.74

Boldareva, E. N., Akimov, V. N., Boichenko, V. A., Stadnichuk, I. N., Moskalenko, A. A., Makhneva, Z. K., et al. (2008). *Rhodobaca barguzinensis* sp. nov., a new alkaliphilic purple nonsulfur bacterium isolated from a soda lake of the Barguzin Valley (Buryat Republic, eastern Siberia). *Mikrobiologiia*, 77(2), 241–254. doi:10.1134/S0026261708020148

Burne, R. V., and Moore, L. S. (1987). Microbialites: organosedimentary deposits of benthic microbial communities. *Palaios* 2 (3), 241–254. doi:10.2307/3514674

Busarakam, K., Bull, A. T., Trujillo, M. E., Riesco, R., Sangal, V., van Wezel, G. P., et al. (2016). *Modestobacter caceresii* sp. nov., novel *Actinobacteria* with an insight into their adaptive mechanisms for survival in extreme hyper-arid Atacama Desert soils. *Syst. Appl. Microbiol.* 39 (4), 243–251. doi:10.1016/j.syapm.2016.03.007

Butterfield, N. J. (2004). A vaucheriacean alga from the middle neoproterozoic of Spitsbergen: implications for the evolution of Proterozoic eukaryotes and the Cambrian explosion. *Paleobiology* 30 (2), 231–252. doi:10.1666/0094-8373(2004)030<0231:Avaftm>2.0.Co;2

Cabestrero, Ó., and Sanz-Montero, M. E. (2016). Brine evolution in two inland evaporative environments: influence of microbial mats in mineral precipitation. *J. Paleolimnol.* 59 (2), 139–157. doi:10.1007/s10933-016-9908-0

Cabestrero, Ó., Tebes-Cayo, C., Hinman, N. W., and Demergasso, C. (2022). Mineral paragenesis precipitating in salt flat pools of Continental environments replicated in microbial mat microcosms without evaporation. *Minerals* 12 (5), 646. doi:10.3390/min12050646

Callahan, B. J., McMurdie, P. J., Rosen, M. J., Han, A. W., Johnson, A. J., and Holmes, S. P. (2016). DADA2: High-resolution sample inference from Illumina amplicon data. *Nat. Methods* 13 (7), 581–583. doi:10.1038/nmeth.3869

Cámara, B., Souza-Egipsy, V., Ascaso, C., Artieda, O., De Los Ríos, A., and Wierzchos, J. (2016). Biosignatures and microbial fossils in endolithic microbial communities colonizing Ca-sulfate crusts in the Atacama Desert. *Chem. Geol.* 443, 22–31. doi:10.1016/j.chemgeo.2016.09.019

Campbell, B. J., and Cary, S. C. (2004). Abundance of reverse tricarboxylic acid cycle genes in free-living microorganisms at deep-sea hydrothermal vents. *Appl. Environ. Microbiol.* 70 (10), 6282–6289. doi:10.1128/AEM.70.10.6282-6289.2004

Carrier, B. L., Abbey, W. J., Beegle, L. W., Bhartia, R., and Liu, Y. (2019). Attenuation of ultraviolet radiation in rocks and minerals: implications for Mars science. *J. Geophys. Res. Planets* 124 (10), 2599–2612. doi:10.1029/2018je005758

Carrizo, D., Sanchez-Garcia, L., Menes, R. J., and Garcia-Rodriguez, F. (2019). Discriminating sources and preservation of organic matter in surface sediments from five Antarctic lakes in the Fildes Peninsula (King George Island) by lipid biomarkers and compound-specific isotopic analysis. *Sci. Total Environ.* 672, 657–668. doi:10.1016/j.scitotenv.2019.03.459

Carrizo, D., de Dios-Cubillas, A., Sanchez-Garcia, L., Lopez, I., and Prieto-Ballesteros, O. (2022). Interpreting molecular and isotopic biosignatures in methane-derived authigenic carbonates in the light of a potential carbon cycle in the icy moons. *Astrobiology* 22 (5), 552–567. doi:10.1089/ast.2021.0036

Castenholz, R. W. (2001). *Berge's manual of systematic bacteriology, 1*. NY, United States: Springer.

Chong-Díaz, G., Demergasso, C., Urrutia Meza, J., and Vargas A, M. (2020). El Dominio Salino del norte de Chile y sus yacimientos de minerales industriales. *Bol. Soc. Geol. Mex.* 72 (3), A020720. doi:10.18268/BSGM2020v72n3a020720

Clarke, K., and Gorley, R. N. (2006). *PRIMER v6: user manual/tutorial, 29*. Plymouth: PRIMER-E.

Coates, R. C., Podell, S., Korobeynikov, A., Lapidus, A., Pevzner, P., Sherman, D. H., et al. (2014). Characterization of cyanobacterial hydrocarbon composition and distribution of biosynthetic pathways. *PLoS One* 9 (1), e85140. doi:10.1371/journal.pone.0085140

Cody, R. D., and Cody, A. M. (1988). Gypsum nucleation and crystal morphology in analog saline terrestrial environments. *J. Sediment. Res.* 58 (2), 247–255. doi:10.1306/212f8d69-2b24-11d7-8648000102c1865d

Culka, A., Jehlička, J., Ascaso, C., Artieda, O., Casero, C. M., and Wierzchos, J. (2017). Raman microspectrometric study of pigments in melanized fungi from the hyperarid Atacama desert gypsum crust. *J. Raman Spectrosc.*, 48(11), 1487–1493. doi:10.1002/jrs.5137

de Los Rios, A., Valea, S., Ascaso, C., Davila, A., Kastovsky, J., McKay, C. P., et al. (2010). Comparative analysis of the microbial communities inhabiting halite evaporites of the Atacama Desert. *Int. J. Microbiol.* 13 (2), 79–89. doi:10.2436/20.1501.01.113

del Buey, P., Sanz-Montero, M. E., Braissant, O., Cabestrero, Ó., and Visscher, P. T. (2021). The role of microbial extracellular polymeric substances on formation of sulfate minerals and fibrous Mg-clays. *Chem. Geol.* 581, 120403. doi:10.1016/j.chemgeo.2021.120403

Demergasso, C., Chong, G., Galleguillos, P., Escudero, L., Martínez-Alonso, M., and Esteve, I. (2003). Tapetes microbianos del Salar de Llamará, Norte de Chile. *Rev. Chil. Hist. Nat.* 76 (3), 485–499. doi:10.4067/S0716-078X2003000300012

Demergasso, C., Casamayor, E. O., Chong, G., Galleguillos, P., Escudero, L., and Pedrós-Alió, C. (2004). Distribution of prokaryotic genetic diversity in athalassohaline lakes of the Atacama Desert, Northern Chile. *FEMS Microbiol. Ecol.*, 48(1), 57–69. doi:10.1016/j.femsec.2003.12.013

Demergasso, C., Escudero, L., Casamayor, E. O., Chong, G., Balague, V., and Pedros-Alio, C. (2008). Novelty and spatio-temporal heterogeneity in the bacterial diversity of hypersaline Lake Tebenquiche (Salar de Atacama). *Extremophiles* 12 (4), 491–504. doi:10.1007/s00792-008-0153-y

Demergasso, C., Neilson, J. W., Tebes-Cayo, C., Véliz, R., Ayma, D., Laubitz, D., et al. (2023). Hyperarid soil microbial community response to simulated rainfall [Original Research]. *Front. Microbiol.* 14, 1202266. doi:10.3389/fmicb.2023.1202266

Díaz, C., and Maidana, N. (2005). *Diatomeas de los salares de Atacama y Punta Negra, II región Chile*. Santiago, Chile: Centro de Ecología Aplicada.

Didyk, B. M., Simoneit, B. R. T., Brassell, S. C., and Eglinton, G. (1978). Organic geochemical indicators of palaeoenvironmental conditions of sedimentation. *Nature* 272 (5650), 216–222. doi:10.1038/272216a0

DiRuggiero, J., Wierzchos, J., Robinson, C. K., Souterre, T., Ravel, J., Artieda, O., et al. (2013). Microbial colonisation of chasmoendolithic habitats in the hyper-arid zone of the Atacama Desert. *Biogeosciences* 10 (4), 2439–2450. doi:10.5194/bg-10-2439-2013

Duffie, J. A., and Beckman, W. A. (2013). "Solar radiation," in *Solar engineering of thermal processes*, 3–42. doi:10.1002/9781118671603.ch1

Ercilla, O. (2019). Origen y evolución de estromatolitos de yeso en salares del altiplano andino, norte de Chile. *Andean Geol.* 46 (1), 211–222. doi:10.5027/andgeov46n1-3029

Fernandez, A. B., Rasuk, M. C., Visscher, P. T., Contreras, M., Novoa, F., Poire, D. G., et al. (2016). Microbial diversity in sediment ecosystems (evaporites domes, microbial mats, and crusts) of hypersaline laguna tebenquiche, Salar de Atacama, Chile. *Front. Microbiol.* 7, 1284. doi:10.3389/fmicb.2016.01284

Finstad, K., Pfeiffer, M., McNicol, G., Barnes, J., Demergasso, C., Chong, G., et al. (2016). Rates and geochemical processes of soil and salt crust formation in Salars of the Atacama Desert, Chile. *Geoderma*, 284, 57–72. doi:10.1016/j.geoderma.2016.08.020

Foster, J. S., Babilonia, J., Parke-Suosaari, E., and Reid, R. P. (2020). "Stromatolites, biosignatures, and astrobiological implications," in *Astrobiology and cuatro Ciénegas Basin as an analog of early Earth*. Editors V. Souza, A. Segura, and J. S. Foster (Cham, Germany: Springer International Publishing), 89–105. doi:10.1007/978-3-030-46087-7_4

Fuentes, E., Carballeira, R., and Prieto, B. (2021). Role of exposure on the microbial consortiums on historical rural granite buildings. *Appl. Sci.* 11 (9), 3786. doi:10.3390/app11093786

Hayes, J. M. (2001). Fractionation of carbon and hydrogen isotopes in biosynthetic processes. *Rev. Mineral. Geochem.* 43 (1), 225–277. doi:10.2138/gsrmg.43.1.225

Hays, L. E., Graham, H. V., Des Marais, D. J., Hausrath, E. M., Horgan, B., McCollom, T. M., et al. (2017). Biosignature preservation and detection in Mars analog environments. *Astrobiology* 17 (4), 363–400. doi:10.1089/ast.2016.1627

Hinman, N., Cabrol, N., Gulick, V., Warren-Rhodes, K., Tebes, C., Chong, G., et al. (2017). *Initial investigations of endoevaporitic gypsum habitats of Salar de Pajonales, Chile*. Arizona, US: Astrobiology Science Conference. Available online at: https://www.hou.usra.edu/meetings/abscicon2017/eposter/3568.pdf

Hinman, N. W., Hofmann, M. H., Warren-Rhodes, K., Phillips, M. S., Noffke, N., Cabrol, N. A., et al. (2022). Surface morphologies in a Mars-Analog Ca-Sulfate Salar, High Andes, Northern Chile [original research]. *Front. Astron. Space Sci.* 8, 797591. doi:10.3389/fspas.2021.797591

Huang, W., Ertekin, E., Wang, T., Cruz, L., Dailey, M., DiRuggiero, J., et al. (2020). Mechanism of water extraction from gypsum rock by desert colonizing microorganisms. *Proc. Natl. Acad. Sci. U. S. A.* 117 (20), 10681–10687. doi:10.1073/pnas.2001613117

Hughes, K. A., and Lawley, B. (2003). A novel Antarctic microbial endolithic community within gypsum crusts. *Environ. Microbiol.* 5 (7), 555–565. doi:10.1046/j.1462-2920.2003.00439.x

Hugler, M., and Sievert, S. M. (2011). Beyond the Calvin cycle: autotrophic carbon fixation in the ocean. *Ann. Rev. Mar. Sci.* 3 (2011), 261–289. doi:10.1146/annurev-marine-120709-142712

Jahnke, L. L., Turk-Kubo, K. A. N. P. M., Green, S. J., Kubo, M. D., Vogel, M., Summons, R. E., et al. (2014). Molecular and lipid biomarker analysis of

a gypsum-hosted endoevaporitic microbial community. *Geobiology* 12 (1), 62–82. doi:10.1111/gbi.12068

Jehlička, J., Oren, A., Vitek, P., and Wierzchos, J. (2024). Microbial colonization of gypsum: from the fossil record to the present day. *Front. Microbiol.* 15 (1), 1397437. doi:10.3389/fmicb.2024.1397437

Jiang, L., Cai, C., Zhang, Y., Mao, S., Sun, Y., Li, K., et al. (2012). Lipids of sulfate-reducing bacteria and sulfur-oxidizing bacteria found in the *Dongsheng uranium* deposit. *Chin. Sci. Bull.* 57 (11), 1311–1319. doi:10.1007/s11434-011-4955-4

Jones, M. W. M., Flannery, D. T., Hurowitz, J. A., Tice, M. M., Schrank, C. E., Allwood, A. C., et al. (2025). *In situ* crystallographic mapping constrains sulfate precipitation and timing in Jezero Crater, Mars. *Sci. Adv.*, 11(16), eadt3048. doi:10.1126/sciadv.adt3048

Kah, L. C., Stack, K. M., Eigenbrode, J. L., Yingst, R. A., and Edgett, K. S. (2018). Syndepositional precipitation of calcium sulfate in Gale Crater, Mars. *Terra nova.* 30 (6), 431–439. doi:10.1111/ter.12359

Kampf, S. K., and Tyler, S. W. (2006). Spatial characterization of land surface energy fluxes and uncertainty estimation at the Salar de Atacama, Northern Chile. *Adv. Water Resour.* 29 (2), 336–354. doi:10.1016/j.advwatres.2005.02.017

Kaneda, T. (1991). Iso- and anteiso-fatty acids in bacteria: biosynthesis, function, and taxonomic significance. *Microbiol. Rev.* 55 (2), 288–302. doi:10.1128/mr.55.2.288-302.1991

Knoll, A. H., Javaux, E. J., Hewitt, D., and Cohen, P. (2006). Eukaryotic organisms in Proterozoic oceans. *Philos. Trans. R. Soc. Lond., Ser. B Biol. Sci.* 361 (1470), 1023–1038. doi:10.1098/rstb.2006.1843

Lafuente, B., Downs, R. T., Yang, H., and Stone, N. (2015). "1. The power of databases: the RRUFF project," in *Highlights in mineralogical crystallography* (Berlin: De Gruyter O), 1–30. Available online at: https://rruff.info/about/downloads/HMC1-30.pdf.

Li, Z., Hu, W., Huang, S., Huang, Y., Li, F., Wang, Q., et al. (2021). *Acuticoccus mangrovi* sp. nov., with an antibacterial property, isolated from mangrove sediment. *Int. J. Syst. Evol. Microbiol.* 71 (12), 1–8. doi:10.1099/ijsem.0.005137

Li, J., Xiang, S., Li, Y., Cheng, R., Lai, Q., Wang, L., et al. (2024). Arcobacteraceae are ubiquitous mixotrophic bacteria playing important roles in carbon, nitrogen, and sulfur cycling in global oceans. *mSystems* 9 (7), e0051324. doi:10.1128/msystems.00513-24

Liu, X., Li, M., Castelle, C. J., Probst, A. J., Zhou, Z., Pan, J., et al. (2018). Insights into the ecology, evolution, and metabolism of the widespread Woesearchaeotal lineages. *Microbiome* 6 (1), 102. doi:10.1186/s40168-018-0488-2

Madigan, M., Bender, K., Buckley, D., Sattley, W. M., and Stahl, D. (2018). *Brock biology of microorganisms*. 15th ed. NY, United States: Pearson.

Martin, M. (2011). Cutadapt removes adapter sequences from high-throughput sequencing reads. *EMBnet J.* 17 (1), 10–12. doi:10.14806/ej.17.1.200

McKay, C. P., Friedmann, E. I., Gomez-Silva, B., Caceres-Villanueva, L., Andersen, D. T., and Landheim, R. (2003). Temperature and moisture conditions for life in the extreme arid region of the Atacama desert: four years of observations including the El Nino of 1997–1998. *Astrobiology* 3 (2), 393–406. doi:10.1089/153110703769016460

McMurdie, P. J., and Holmes, S. (2013). phyloseq: an R package for reproducible interactive analysis and graphics of microbiome census data. *PLoS One* 8 (4), e61217. doi:10.1371/journal.pone.0061217

MR DNA (2019). Shallowater, TX, USA. Available online at: www.mrdnafreesoftware.com (Accessed December 6).

Mukaiyama, K., Jung, J. W., Sepehri-Amin, H., Kasai, S., Furubayashi, T., Ohkubo, T., et al. (2019). Over 100% magnetoresistance ratio at room temperature in magnetic tunnel junctions with CuGaSe2 spacer layer. *Appl. Phys. Lett.* 114 (17), 172402. doi:10.1063/1.5092269

Naranjo, J. A., Villa, V., and Venegas, C. (2013). *Geología de las áreas Salar de Pajonales y Cerro Moño, regiones de Antofagasta y Atacama*. Santiago: Sernageomin. Available online at: https://repositorio.sernageomin.cl/handle/0104/18723.

Nemeckova, K., Mares, J., Prochazkova, L., Culka, A., Kosek, F., Wierzchos, J., et al. (2023). Gypsum endolithic phototrophs under moderate climate (Southern Sicily): their diversity and pigment composition. *Front. Microbiol.* 14, 1175066. doi:10.3389/fmicb.2023.1175066

Noffke, N. (2021). Microbially induced sedimentary structures in clastic deposits: implication for the prospection for fossil life on Mars. *Astrobiology* 21 (7), 866–892. doi:10.1089/ast.2021.0011

Núñez Salazar, R., Aguirre, C., Soto, J., Salinas, P., Salinas, C., Prieto, H., et al. (2020). Physicochemical parameters affecting the distribution and diversity of the water column microbial community in the high-altitude andean lake system of La Brava and La Punta. *Microorganisms* 8 (8), 1181. doi:10.3390/microorganisms8081181

Oehlert, A. M., Suosaari, E. P., Kong, T., Piggot, A. M., Maizel, D., Lascu, I., et al. (2022). Physical, chemical, and microbial feedbacks controlling brine geochemistry and lake morphology in polyextreme salar environments. *Sci. Total Environ.* 836, 155378. doi:10.1016/j.scitotenv.2022.155378

Oliveros, J. C. (2007). Venny. An interactive tool for comparing lists with Venn's diagrams. (Madrid: BioinfoGP Service, Centro Nacional de Biotecnologia (CNB-CSIC)). Available online at: https://bioinfogp.cnb.csic.es/tools/venny/ (Accessed July 12, 2023).

Oshone, R., Ngom, M., Chu, F., Mansour, S., Sy, M. O., Champion, A., et al. (2017). Genomic, transcriptomic, and proteomic approaches towards understanding the molecular mechanisms of salt tolerance in Frankia strains isolated from Casuarina trees. *BMC Genomics* 18 (1), 633. doi:10.1186/s12864-017-4056-0

Pellegrino, L., Natalicchio, M., Cotellucci, A., Genre, A., Jordan, R. W., Carnevale, G., et al. (2024). The impact of early diagenesis on biosignature preservation in sulfate evaporites: insights from Messinian (Late Miocene) gypsum. *Geobiology* 22 (6), e70007. doi:10.1111/gbi.70007

Perkerson, R. B., Johansen, J. R., Kovacik, L., Brand, J., Kastovsky, J., and Casamatta, D. A. (2011). A unique Pseudanabaenalean (*Cyanobacteria*) Genus Nodosilinea Gen. Nov. based on morphological and molecular Data(1). *J. Phycol.* 47 (6), 1397–1412. doi:10.1111/j.1529-8817.2011.01077.x

Perl, S., Adeli, S., Basu, C., Baxter, B. K., Bowman, J., Boyd, E., et al. (2021). Salty Environments: the importance of evaporites and brine environments as habitats and preservers of biosignatures. *Bull. Am. Astron. Soc.* 53 (4), 240. doi:10.3847/25c2cfeb.d0fffbba

Perri, E., and Spadafora, A. (2011). "Evidence of microbial biomineralization in modern and ancient stromatolites," in *Stromatolites: interaction of microbes with sediments* (Dordrecht, The Netherlands: Springer), 631–649. doi:10.1007/978-94-007-0397-1_28

Petrash, D. A., Gingras, M. K., Lalonde, S. V., Orange, F., Pecoits, E., and Konhauser, K. O. (2012). Dynamic controls on accretion and lithification of modern gypsum-dominated thrombolites, Los Roques, Venezuela. *Sediment. Geol.* 245-246, 29–47. doi:10.1016/j.sedgeo.2011.12.006

Pfeiffer, M., Morgan, A., Heimsath, A., Jordan, T., Howard, A., and Amundson, R. (2021). Century scale rainfall in the absolute Atacama Desert: landscape response and implications for past and future rainfall. *Quat. Sci. Rev.* 254, 106797. doi:10.1016/j.quascirev.2021.106797

Phua, Y. Y., Ehlmann, B. L., Siljeström, S., Czaja, A. D., Beck, P., Connell, S., et al. (2024). Characterizing hydrated sulfates and altered phases in Jezero Crater fan and floor geologic units with SHERLOC on Mars 2020. *J. Geophys. Res. Planets* 129 (7), e2023JE008251. doi:10.1029/2023JE008251

Pointing, S. B., Warren-Rhodes, K. A., Lacap, D. C., Rhodes, K. L., and McKay, C. P. (2007). Hypolithic community shifts occur as a result of liquid water availability along environmental gradients in China's hot and cold hyperarid deserts. *Environ. Microbiol.* 9 (2), 414–424. doi:10.1111/j.1462-2920.2006.01153.x

Preuß, A., Schauder, R., Fuchs, G., and Stichler, W. (1989). Carbon isotope fractionation by autotrophic bacteria with three different Co_2 fixation pathways. *Z. für Naturforsch. C* 44 (5-6), 397–402. doi:10.1515/znc-1989-5-610

Pueyo, J. J., Demergasso, C., Escudero, L., Chong, G., Cortéz-Rivera, P., Sanjurjo-Sánchez, J., et al. (2021). On the origin of saline compounds in acidic salt flats (Central Andean Altiplano). *Chem. Geol.* 574 (120155), 1–25. doi:10.1016/j.chemgeo.2021.120155

Quast, C., Pruesse, E., Yilmaz, P., Gerken, J., Schweer, T., Yarza, P., et al. (2013). The SILVA ribosomal RNA gene database project: improved data processing and web-based tools. *Nucleic Acids Res.* 41 (Database issue), D590–D596. doi:10.1093/nar/gks1219

R Core Team (2024). R: a language and environment for statistical computing (Vienna: R Foundation for Statistical Computing). Available online at: https://www.R-project.org/ (Accessed September 18, 2024).

Ramos-Tapia, I., Nunez, R., Salinas, C., Salinas, P., Soto, J., and Paneque, M. (2022). Study of Wetland Soils of the Salar de Atacama with different azonal vegetative formations reveals changes in the microbiota associated with hygrophile plant type on the soil surface. *Microbiol. Spectr.* 10 (5), e0053322. doi:10.1128/spectrum.00533-22

Rampe, E. B., Blake, D. F., Bristow, T. F., Ming, D. W., Vaniman, D. T., Morris, R. V., et al. (2020). Mineralogy and geochemistry of sedimentary rocks and eolian sediments in Gale crater, Mars: a review after six Earth years of exploration with Curiosity. *Geochem.* 80 (2), 125605. doi:10.1016/j.chemer.2020.125605

Rasuk, M. C., Kurth, D., Flores, M. R., Contreras, M., Novoa, F., Poire, D., et al. (2014). Microbial characterization of microbial ecosystems associated to evaporites domes of gypsum in Salar de Llamara in Atacama desert. *Microb. Ecol.* 68 (3), 483–494. doi:10.1007/s00248-014-0431-4

Reid, R. P., Oehlert, A. M., Suosaari, E. P., Demergasso, C., Chong, G., Escudero, L. V., et al. (2021). Electrical conductivity as a driver of biological and geological spatial heterogeneity in the Puquios, Salar de Llamara, Atacama Desert, Chile. *Sci. Rep.* 11 (1), 12769. doi:10.1038/s41598-021-92105-2

Révész, K., Qi, H., and Coplan, T. B. (2012). Determination of the δ 15 N and δ 13 C of total nitrogen and carbon in solids; RSIL lab code 1832 [Slightly Revised from Version 1.1 Released in 2007](2328-7055) (Reston, VA: Geological Survey). Available online at: https://pubs.usgs.gov/tm/2006/tm10c10/ (Accessed September 17, 2012).

Rhind, T., Ronholm, J., Berg, B., Mann, P., Applin, D., Stromberg, J., et al. (2014). Gypsum-hosted endolithic communities of the Lake St. Martin impact structure, Manitoba, Canada: spectroscopic detectability and implications for Mars. *Int. J. Astrobiol.* 13 (4), 366–377. doi:10.1017/S1473550414000378

Risacher, F., Alonso, H., and Salazar, C. (1999). Geoquímica de aguas en cuencas cerradas: i, II y III regiones-Chile. Volumen III Estudio de cuencas de la II Región. Available online at: snia.mop.gob.cl/repositoriodga/

Risacher, F., Alonso, H., and Salazar, C. (2003). The origin of brines and salts in Chilean salars: a hydrochemical review. *Earth-Sci. Rev.*, 63(3-4), 249–293. doi:10.1016/S0012-8252(03)00037-0

Robson, J. N., and Rowland, S. J. (1993). Synthesis, chromatographic and spectral characterisation of 2,6,11,15-tetramethylhexadecane (crocetane) and 2,6,9,13-tetramethyltetradecane: reference acyclic isoprenoids for geochemical studies. *Org. Geochem.* 20 (7), 1093–1098. doi:10.1016/0146-6380(93)90117-t

Rodríguez, C. (2018). *Geología del Salar Pajonales (7209000-7226500N 510000-530 000E) y Antecedentes de su Microbiota, Antofagasta, Norte de Chile*. Antofagasta, Chile: Universidad Católica del Norte.

Roldán, M., Ascaso, C., and Wierzchos, J. (2014). Fluorescent fingerprints of endolithic phototrophic *Cyanobacteria* living within halite rocks in the Atacama Desert. *Appl. Environ. Microbiol.* 80 (10), 2998–3006. doi:10.1128/AEM.03428-13

Rontani, J.-F., and Volkman, J. K. (2005). Lipid characterization of coastal hypersaline cyanobacterial mats from the Camargue (France). *Org. Geochem.* 36 (2), 251–272. doi:10.1016/j.orggeochem.2004.07.017

Rouchy, J. M., and Monty, C. (2000). "Gypsum microbial sediments: Neogene and modern examples," in *Microbial sediments* (Berlin, Heidelberg: Springer Berlin Heidelberg), 209–216. doi:10.1007/978-3-662-04036-2_23

Sanchez-Garcia, L., Fernandez-Martinez, M. A., Garcia-Villadangos, M., Blanco, Y., Cady, S. L., Hinman, N., et al. (2018). Microbial biomarker transition in high-altitude sinter mounds from El tatio (Chile) through different stages of hydrothermal activity. *Front. Microbiol.* 9, 3350. doi:10.3389/fmicb.2018.03350

Sanchez-Garcia, L., Fernandez-Martinez, M. A., Moreno-Paz, M., Carrizo, D., Garcia-Villadangos, M., Manchado, J. M., et al. (2020). Simulating Mars drilling mission for searching for life: ground-truthing lipids and other complex microbial biomarkers in the iron-sulfur rich rio Tinto analog. *Astrobiology* 20 (9), 1029–1047. doi:10.1089/ast.2019.2101

Sanz-Montero, M. E., Rodriguez-Aranda, J. P., and Calvo, J. P. (2006). Mediation of endoevaporitic microbial communities in early replacement of gypsum by dolomite: a case study from Miocene Lake deposits of the Madrid Basin, Spain. *J. Sediment. Res.* 76 (12), 1257–1266. doi:10.2110/jsr.2006.122

Schopf, J. W., Farmer, J. D., Foster, I. S., Kudryavtsev, A. B., Gallardo, V. A., and Espinoza, C. (2012). Gypsum-permineralized microfossils and their relevance to the search for life on Mars. *Astrobiology* 12 (7), 619–633. doi:10.1089/ast.2012.0827

Shiea, J., Brassell, S. C., and Ward, D. M. (1990). Mid-chain branched mono- and dimethyl alkanes in hot spring cyanobacterial mats: a direct biogenic source for branched alkanes in ancient sediments? *Org. Geochem.* 15 (3), 223–231. doi:10.1016/0146-6380(90)90001-g

Shin, Y., and Brangwynne, C. P. (2017). Liquid phase condensation in cell physiology and disease. *Science* 357 (6357), 3812–3818. doi:10.1126/science.aaf4382

Siljeström, S., Czaja, A. D., Corpolongo, A., Berger, E. L., Li, A. Y., Cardarelli, E., et al. (2024). Evidence of sulfate-rich fluid alteration in Jezero crater floor, Mars. *J. Geophys. Res. Planets* 129 (1), e2023JE007989. doi:10.1029/2023je007989

Sorokin, D. Y., Abbas, B., Merkel, A. Y., Rijpstra, W. I. C., Damste, J. S. S., Sukhacheva, M. V., et al. (2015). *Methanosalsum natronophilum* sp. nov., and *Methanocalculus alkaliphilus* sp. nov., haloalkaliphilic methanogens from hypersaline soda lakes. *Int. J. Syst. Evol. Microbiol.* 65 (10), 3739–3745. doi:10.1099/ijsem.0.000488

Taher, A. G. (2014). Formation and calcification of modern gypsum-dominated stromatolites, EMISAL, Fayium, Egypt. *Facies* 60 (3), 721–735. doi:10.1007/s10347-014-0405-5

Tamura, K., Stecher, G., and Kumar, S. (2021). MEGA11: molecular evolutionary genetics analysis version 11. *Mol. Biol. Evol.* 38 (7), 3022–3027. doi:10.1093/molbev/msab120

Taylor, J., and Parkes, R. J. (1983). The cellular fatty acids of the sulphate-reducing bacteria, *Desulfobacter* sp., *Desulfobulbus* sp. and *Desulfovibrio desulfuricans*. *Microbiology* 129 (11), 3303–3309. doi:10.1099/00221287-129-11-3303

Thompson, J. B., and Ferris, F. G. (1990). Cyanobacterial precipitation of gypsum, calcite, and magnesite from natural alkaline lake water. *Geology* 18 (10), 995–998. doi:10.1130/0091-7613(1990)018<0995:Cpogca>2.3.Co;2

Thompson, J. D., Gibson, T. J., and Higgins, D. G. (2002). "Multiple sequence alignment using ClustalW and ClustalX," in *Current Protocols in Bioinformatics, Chapter 2, Unit 2 3*. doi:10.1002/0471250953.bi0203s00

Tsubouchi, T., Ohta, Y., Haga, T., Usui, K., Shimane, Y., Mori, K., et al. (2014). *Thalassospira alkalitolerans* sp. nov. and *Thalassospira mesophila* sp. nov., isolated from a decaying bamboo sunken in the marine environment, and emended description of the genus Thalassospira. *Int. J. Syst. Evol. Microbiol.* 64 (Pt 1), 107–115. doi:10.1099/ijs.0.056028-0

United Nations Environment Programme (1992). *World atlas of desertification*. Edward Arnold. Available online at: wedocs.unep.org/20.500.11822/42137

Valdivia-Silva, J. E., Karouia, F., Navarro-Gonzalez, R., and McKay, C. (2016). Microorganisms, organic carbon, and their relationship with oxidant activity in hyper-arid Mars-like soils implications for soil habitability. *Palaios* 31 (1), 1–9. doi:10.2110/palo.2015.010

van der Meer, M. T., Schouten, S., de Leeuw, J. W., and Ward, D. M. (2000). Autotrophy of green non-sulphur bacteria in hot spring microbial mats: biological explanations for isotopically heavy organic carbon in the geological record. *Environ. Microbiol.* 2 (4), 428–435. doi:10.1046/j.1462-2920.2000.00124.x

Van Driessche, A. E. S., Stawski, T. M., and Kellermeier, M. (2019). Calcium sulfate precipitation pathways in natural and engineered environments. *Chem. Geol.* 530, 119274. doi:10.1016/j.chemgeo.2019.119274

Vaniman, D. T., Martínez, G. M., Rampe, E. B., Bristow, T. F., Blake, D. F., Yen, A. S., et al. (2018). Gypsum, bassanite, and anhydrite at Gale crater, Mars. *Am. Min.*, 103(7), 1011–1020. doi:10.3390/min14080815

Vargas, C., Jebbar, M., Carrasco, R., Blanco, C., Calderon, M. I., Iglesias-Guerra, F., et al. (2006). Ectoines as compatible solutes and carbon and energy sources for the halophilic bacterium *Chromohalobacter salexigens*. *J. Appl. Microbiol.* 100 (1), 98–107. doi:10.1111/j.1365-2672.2005.02757.x

Vignale, F. A., Kurth, D., Lencina, A. I., Poire, D. G., Chihuailaf, E., Munoz-Herrera, N. C., et al. (2021). Geobiology of Andean microbial ecosystems discovered in Salar de Atacama, Chile. *Front. Microbiol.* 12, 762076. doi:10.3389/fmicb.2021.762076

Vogel, M. B., Des Marais, D. J., Parenteau, M. N., Jahnke, L. L., Turk, K. A., and Kubo, M. D. Y. (2010). Biological influences on modern sulfates: textures and composition of gypsum deposits from Guerrero Negro, Baja California Sur, Mexico. *Sediment. Geol.* 223 (3-4), 265–280. doi:10.1016/j.sedgeo.2009.11.013

Volkman, J. K. (1986). A review of sterol markers for marine and terrigenous organic matter. *Org. Geochem.* 9 (2), 83–99. doi:10.1016/0146-6380(86)90089-6

Volkman, J. K., Barrett, S. M., Blackburn, S. I., Mansour, M. P., Sikes, E. L., and Gelin, F. (1998). Microalgal biomarkers: a review of recent research developments. *Org. Geochem.* 29 (5-7), 1163–1179. doi:10.1016/s0146-6380(98)00062-x

Walker, C. B., de la Torre, J. R., Klotz, M. G., Urakawa, H., Pinel, N., Arp, D. J., et al. (2010). Nitrosopumilus maritimus genome reveals unique mechanisms for nitrification and autotrophy in globally distributed marine crenarchaea. *Proc. Natl. Acad. Sci. U. S. A.* 107 (19), 8818–8823. doi:10.1073/pnas.0913533107

Warren, J. K. (2006). *Evaporites: sediments, resources and hydrocarbons*. Berlin, Heidelberg: Springer. doi:10.1007/3-540-32344-9

Warren-Rhodes, K. A., Rhodes, K. L., Pointing, S. B., Ewing, S. A., Lacap, D. C., Gomez-Silva, B., et al. (2006). Hypolithic Cyanobacteria, dry limit of photosynthesis, and microbial ecology in the hyperarid Atacama Desert. *Microb. Ecol.* 52 (3), 389–398. doi:10.1007/s00248-006-9055-7

Warren-Rhodes, K., Cabrol, N. A., Phillips, M., Tebes-Cayo, C., Kalaitzis, F., Ayma, D., et al. (2023). Orbit-to-ground framework to decode and predict biosignature patterns in terrestrial analogues. *Nat. Astron.* 7 (4), 406–422. doi:10.1038/s41550-022-01882-x

Wierzchos, J., Ascaso, C., and McKay, C. P. (2006). Endolithic *Cyanobacteria* in halite rocks from the hyperarid core of the Atacama Desert. *Astrobiology* 6 (3), 415–422. doi:10.1089/ast.2006.6.415

Wierzchos, J., DiRuggiero, J., Vitek, P., Artieda, O., Souza-Egipsy, V., Skaloud, P., et al. (2015). Adaptation strategies of endolithic chlorophototrophs to survive the hyperarid and extreme solar radiation environment of the Atacama Desert [original research]. *Front. Microbiol.* 6, 934. doi:10.3389/fmicb.2015.00934

WRPLOT (2021). *WRPLOT view™ freeware: wind rose plots for meteorological data. In (Version 8.0.2) [Software WRPLOT]*. Lakes Environmental Software. Available online at: https://www.weblakes.com/products/wrplot/index.html.

Ziolkowski, L. A., Mykytczuk, N. C. S., Omelon, C. R., Johnson, H., Whyte, L. G., and Slater, G. F. (2013a). Arctic Gypsum endoliths: a biogeochemical characterization of a viable and active microbial community. *Biogeosci. Disc.* 10, 2269–2304. doi:10.5194/bgd-10-2269-2013

Ziolkowski, L. A., Wierzchos, J., Davila, A. F., and Slater, G. F. (2013b). Radiocarbon evidence of active endolithic microbial communities in the hyperarid core of the Atacama Desert. *Astrobiology* 13 (7), 607–616. doi:10.1089/ast.2012.0854

Zorzano, M.-P., Martínez, G., Polkko, J., Tamppari, L. K., Newman, C., Savijärvi, H., et al. (2024). Present-day thermal and water activity environment of the Mars Sample Return collection. *Sci. Rep.*, 14(1), 7175. doi:10.1038/s41598-024-57458-4